

# White dwarfs within 13 pc: Insights from ultraviolet spectroscopy

Mairi W. O’Brien<sup>1\*</sup>, Pier-Emmanuel Tremblay<sup>1</sup>, Boris T. Gänsicke<sup>1</sup>, Mark A. Hollands<sup>1</sup>, Detlev Koester<sup>2</sup>, Snehalata Sahu<sup>1</sup>, Antoine Bédard<sup>1</sup>, Andrew M. Buchan<sup>1</sup>, Tim Cunningham<sup>3</sup>, John H. Debes<sup>4</sup>, J. J. Hermes<sup>5</sup> and Piotr M. Kowalski<sup>6</sup>

<sup>1</sup> Department of Physics, University of Warwick, Coventry CV4 7AL, UK

<sup>2</sup> Institut für Theoretische Physik und Astrophysik, University of Kiel, 24098 Kiel, Germany

<sup>3</sup> Center for Astrophysics, Harvard & Smithsonian, 60 Garden St., Cambridge, MA 02138, USA

<sup>4</sup> ESA for AURA, The Space Telescope Science Institute, 3700 San Martin Dr., Baltimore, MD 21218, USA

<sup>5</sup> Department of Astronomy & Institute for Astrophysical Research, Boston University, Boston, MA 02215, USA

<sup>6</sup> Institute of Energy Technologies – Theory and Computation of Energy Materials (IET-3), Forschungszentrum Jülich GmbH, 52425 Jülich, Germany

Accepted XXX. Received YYY; in original form 2026-07-07

## ABSTRACT

We present a comprehensive multi-wavelength spectroscopic and photometric analysis of the 44 confirmed white dwarfs within 13 pc of the Sun. Combining flux-calibrated ultraviolet (UV) spectroscopy from the *Hubble Space Telescope* (STIS and COS) with ground-based optical spectroscopy, as well as photometry from *Gaia*, 2MASS, and WISE, we employ a hybrid fitting method to calculate atmospheric parameters. Each white dwarf was fitted with a bespoke model depending on its detailed atmospheric composition, aside from two strongly magnetic stars. We find a systematic discrepancy in H-atmosphere white dwarfs with  $T_{\text{eff}} < 10\,000$  K, where fits incorporating UV spectra result in effective temperatures that are 2–6 per cent higher than those derived from optical and infrared photometry alone. We re-classify three He-rich white dwarfs as metal enriched following a magnesium detection in their near-UV spectra: WD 0435–088, WD 1132–325 and WD 1917+386. In total, we identify six stars in the sample for which metals were only detected in the UV. Overall we find that 30 per cent of the 13 pc white dwarfs show spectroscopic evidence of evolved planetary systems. Our analysis revealed no measurable difference between the hydrogen content of DQ and DC white dwarfs, although the upper limits of carbon in DCs are significantly below that of the DQ population. We find a multiplicity fraction of 32 per cent for the 13 pc white dwarfs.

**Key words:** ultraviolet: stars – white dwarfs – stars: statistics – solar neighbourhood

## 1 INTRODUCTION

White dwarfs are the evolutionary endpoint of 95 per cent of all stars. Despite the recent discoveries of hundreds of thousands of white dwarf candidates with the *Gaia* mission (Gaia Collaboration et al. 2021; Gentile Fusillo et al. 2021), even those in our immediate Solar neighbourhood remain incompletely characterised across all wavelengths. The white dwarfs in the local volume exhibit a wide diversity of masses, ages, atmospheric compositions (including evidence of evolved planetary systems), multiplicity, and magnetic field strengths. Volume-limited studies provide a critical insight into white dwarf cooling rates, evolution of planetary systems, and the roles of binarity and magnetic fields in stellar evolution (Holberg et al. 2002, 2008; Giammichele et al. 2012; Toonen et al. 2017; Hollands et al. 2018b; Bagnulo & Landstreet 2022; Caron et al. 2023; O’Brien et al. 2024; Kilic et al. 2025; Ould Rouis et al. 2026).

Optical spectroscopy of white dwarfs is commonplace, and enables an initial characterisation of atmospheric properties including chemical composition. Ultraviolet (UV) observations provide new insights into a star. Some photospheric metal absorption lines that

are not visible in the optical appear in the UV (Weidemann et al. 1980; Koester & Wolff 2000; Gänsicke et al. 2012; Jura et al. 2012; Sahu et al. 2024), enabling the characterisation of the geochemistry of accreted planetesimals (Koester et al. 2014) or constraining the convective dredge-up of carbon from the interior (Bédard 2024; Sahu et al. 2025a). In addition to chemical composition, the UV continuum flux enables models to be fitted over a larger wavelength range to better constrain the stellar parameters such as mass, surface gravity ( $\log g$ ), effective temperature ( $T_{\text{eff}}$ ) and age (Lajoie & Bergeron 2007; Sahu et al. 2023; Elms et al. 2024).

Most previous spectroscopic UV white dwarf surveys have focused on warmer ( $T_{\text{eff}} \gtrsim 10\,000$  K) objects that are bluer, brighter and have more lines in this wavelength range. White dwarfs warmer than 10 000 K represent just 15 per cent of the local volume (O’Brien et al. 2024). The white dwarf temperature distribution in the local volume is primarily a function of white dwarf cooling rates, which map the population back to the underlying convolution of the initial mass function and the star formation history of the Milky Way. Cooler and older white dwarfs emit less flux in the near-UV, and as such have not been studied extensively at UV wavelengths. Spectroscopic UV observations of cool white dwarfs are key to test various aspects of

\* E-mail: mairi.obrien1@gmail.com

white dwarf physics and metal accretion (Wolff et al. 2002; Saumon et al. 2014; Hollands et al. 2022)

The high-density atmospheres of the coolest white dwarfs are notoriously challenging to model (Saumon & Jacobson 1999; Bergeron et al. 2001), particularly regarding collision induced absorption (CIA) in the infrared (Blouin et al. 2017; Elms et al. 2022; Bergeron et al. 2022; Saumon et al. 2022; Blouin et al. 2024). The accurate modelling of cool white dwarf atmospheres is a significant issue that affects most of the local white dwarf population, as over half of local white dwarfs are cooler than 6000 K (O’Brien et al. 2024). Improved Ly  $\alpha$  broadening profiles from Kowalski & Saumon (2006); Allard & Kielkopf (2009); Saumon et al. (2014); Sahu et al. (2025b) showed that the Ly  $\alpha$  line is collision-broadened into the blue part of the optical. Line profiles used in the modelling perform well (Saumon et al. 2014), and this broadening is caused mostly by H–H<sub>2</sub> and H–He collisions. However, even with the well tested and validated Ly  $\alpha$  opacities for the UV and optical, and CIA opacities in the infrared, there are still subtle discrepancies between the predicted and observed photometry and spectral energy distributions, visible in analysis of large data sets (O’Brien et al. 2024).

In this work, we present a detailed analysis of UV spectroscopy from the *Hubble Space Telescope* (*HST*) of white dwarfs within 13 pc of the Sun, some of our nearest stellar neighbours. Given their proximity, white dwarfs within 13 pc are among the brightest members of their spectral types, providing uniquely high-quality data for atmospheric modelling. The 13 pc UV observations have been supplemented with medium-resolution optical spectroscopy. We combined the STIS data, which is flux-calibrated up to the 1 per cent level (Bohlin et al. 2019), with optical and IR photometry from *Gaia* DR3 (Gaia Collaboration et al. 2021), the Two Micron All-Sky Survey (2MASS) (Skrutskie et al. 2006) and the Wide-field Infrared Survey Explorer (WISE) (Wright et al. 2010). We then performed spectrophotometric fits from the UV to the IR incorporating the STIS spectra plus the photometry, as well as fits to spectral features to determine atmospheric compositions.

By fitting multi-wavelength flux-calibrated data across the UV-to-IR range, there is an immediate visual insight into discrepancies and offsets between the fits to different regions of the white dwarf continuum. In this work, we provide best-fitting parameters for every 13 pc white dwarf, and discuss the differences between these fits in different wavelength regimes. The UV spectra enable us to determine precise limits on carbon and hydrogen in DC white dwarfs and hydrogen in DQ white dwarfs. We also test the impact of fitting magnetic DA white dwarfs with radiative models instead of convective models. We discuss the binary population and photometric variability within the 13 pc sample, and additionally provide insight into the geology of the material accreting onto 13 pc white dwarfs.

## 2 OBSERVATIONS

There are 44 spectroscopically confirmed white dwarfs known to be within 13 pc of the Sun (O’Brien et al. 2024). These reside in 42 stellar systems, comprising 28 isolated white dwarfs and 14 multiple-star systems containing at least one white dwarf (of which two are WD + WD binaries). The details of the observations of the white dwarfs that were analysed in this work are listed in Table 1. *HST* observations of 36 targets within 13 pc were conducted during Cycle 23 (program 14076; Gänsicke et al. 2015), with the Space Telescope Imaging Spectrograph (STIS) and the Cosmic Origins Spectrograph (COS). All of the Cycle 23 observations were completed between November 2015 and January 2017.

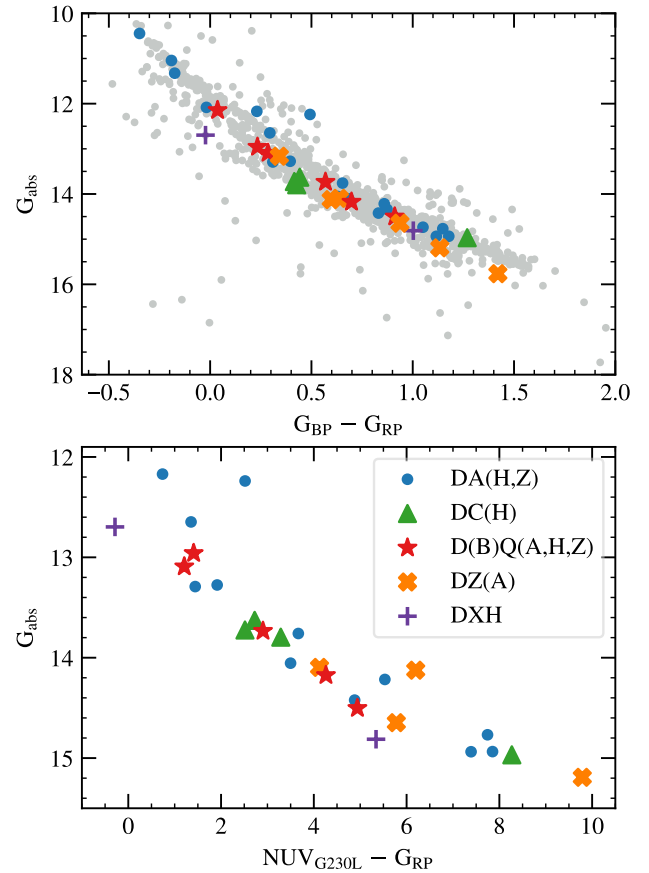


**Figure 1.** HR diagrams for the 13 pc white dwarf sample, separated by spectral type. *Top:* A *Gaia* HR diagram using the G, G<sub>BP</sub> and G<sub>RP</sub> bands. The grey points are white dwarfs within 40 pc (O’Brien et al. 2024). *Bottom:* A *Gaia* HR diagram with newly created NUV<sub>G230L</sub> photometric points. The NUV<sub>G230L</sub> colour was generated by convolving the STIS G230L spectra with the GALEX NUV filter. Only white dwarfs with G230L observations are shown in this lower plot.

WD 0727+482 A+B is a white dwarf + white dwarf binary with a separation of 0.66 arcsec. For the Cycle 23 STIS G230L observation, both stars were positioned along the 52"×2" long-slit, and were later extracted individually. Shorter slits were used for three of the Cycle 23 STIS G230L observations to limit contamination from a nearby companion star. WD 0208–510 has a 2.1 arcsec separation from a K dwarf (GJ 86 A), and was observed with the 52"×0.2" aperture. WD 0426+588 has a 9.0 arcsec separation from an M dwarf (Stein 2051 A), and was observed with the 52"×0.5" aperture. WD 1132–325 has a 15 arcsec separation from a K dwarf (GJ 432 A), and was also observed with the 52"×0.5" aperture. Additional archival *HST* observations were compiled in this work to improve the completeness of the 13 pc sample. Details of program IDs are in Table 1.

Eighteen white dwarfs within 13 pc were observed with the X-shooter spectrograph on the VLT (Vernet et al. 2011). The data were reduced using the REFLEX pipeline (Freudling et al. 2013), and we performed telluric corrections using MOLECFIT (Kausch et al. 2015; Smette et al. 2015). Four white dwarfs have archival UVES data, and reduction was carried out using the same procedure. Six white dwarfs were observed with the ISIS instrument on the WHT. All of the WHT

ISIS observations were taken on 2016 September 04. Some additional optical spectra were taken from the Montréal White Dwarf Database (Dufour et al. 2017), and the references to the original publications of these spectra are found in Table 1.

Four confirmed white dwarfs within the 13 pc volume do not have *HST* UV spectra available. WD 0810–353, WD 1630+089 and WD 2150+591 were discovered to be within 13 pc by *Gaia*, years after the Cycle 23 program, and have therefore not yet been observed in the UV with *HST*. WD 2251–070 was observed with STIS G230L over three orbits as part of the Cycle 23 program but it is so faint in the UV that there was no detection. The white dwarf in the post-common envelope binary system G 203–47 was directly observed in an *HST* STIS G230L spectra by O’Brien et al. (in press), and was found to be  $\approx 5300$  K. The UV spectrum of G 203–47 is not analysed further in this work.

All 13 pc white dwarfs analysed in this work were checked for magnetism using sensitive spectropolarimetric measurements, as part of the larger 20 pc volume sample (Bagnulo & Landstreet 2021). All spectral types in Table 2 account for this magnetic field search, with an ‘H’ at the end of the spectral type indicating a magnetic field detection of any kind. Additionally, eight members of the 13 pc sample were observed by Zuckerman et al. (2003) at a resolution of 34 000 around the Ca II H and K doublet, providing calcium abundance detections and upper limits for H-atmosphere white dwarfs. The remaining members of the sample could have weak metal features and should be followed up with a high-resolution optical spectrograph. The spectral types in Table 2 are based on the Sion et al. (1983) naming system, and are up-to-date following our analysis. For simplicity, due to our multi-wavelength dataset, we opted to combine UV and optical features for an overall spectral type classification.

### 3 MODEL ATMOSPHERES AND FITTING

The coolest white dwarfs within 13 pc have almost no flux in the STIS G230L band, except for the reddest end. When fitted in isolation with atmosphere models, these cool STIS spectra do not provide meaningful white dwarf parameters, and as such, additional optical and IR photometry was required to constrain their parameters. For this reason, we employed a universal hybrid fitting method, where STIS spectra, together with *Gaia* DR3  $G$ ,  $G_{BP}$ ,  $G_{RP}$ , 2MASS  $J$ ,  $H$ ,  $K_s$  and WISE  $W1$ ,  $W2$  photometry were combined into a hybrid spectrophotometric fit, to obtain atmospheric parameters, including  $T_{\text{eff}}$  and  $\log g$ , as well as mass and radius. This method constrains parameters of the coolest members of the sample well, and the fit was not weighted in favour of any particular dataset.

The STIS spectra are flux-calibrated at the 1–2 per cent level (Elms et al. 2024), and *Gaia* DR3  $G$ ,  $G_{BP}$ ,  $G_{RP}$ , and 2MASS  $J$ ,  $H$ ,  $K_s$  and WISE  $W1$ ,  $W2$  photometry are also well flux-calibrated. This flux calibration enables a precise full continuum fit. We elected not to incorporate Pan-STARRS *grizy* and SDSS *ugriz* optical photometry in the fits, because many of the 13 pc white dwarfs were so bright that they saturated in multiple Pan-STARRS and SDSS filters, and we wanted a uniform sample of uncontaminated photometry. Additionally, *Gaia* has proven to be as precise and accurate as Pan-STARRS and SDSS for local white dwarfs (O’Brien et al. 2024). The parallax of each star was fixed to the *Gaia* DR3 value during the fit. We assumed the distance to be the inverse of the parallax, which is appropriate for these sources as their *Gaia* `parallax_over_error`  $> 1800$ , and therefore they have a negligible measurement error (Bailer-Jones 2015).

The STIS E140M and E230M observations initially suffered from

echelle order ripples, which were corrected using the STISBLAZEPIX package from Baer et al. (2018) before fitting. The atomic line data used to identify spectral features in this work were obtained from NIST (Kramida et al. 2018). Photospheric lines (from accreted metals) and interstellar lines (from gas in the line of sight) are usually offset due to the white dwarf gravitational redshift, and the STIS E140M/H and E230M/H gratings have a high enough resolution that the narrow photospheric lines and interstellar lines are resolved. The line components of Si II 1265 Å have a lower energy level of 0.035 eV, corresponding to  $\approx 400$  K. These levels are not populated in the cool interstellar medium, and so all lines with the same radial velocity as the Si II 1265 Å line must be photospheric. Interstellar lines were identified and then fitted with a Gaussian using a least squares fitting method, or in the case of the two components in WD 0642–166 (Sirius B), two Gaussians. The regions of the interstellar lines were then masked from the spectra prior to fitting.

#### 3.1 H-atmosphere fitting

We fitted H-atmosphere white dwarf data with updated 3D local thermodynamic equilibrium (LTE) model spectra<sup>1</sup> from Tremblay et al. (2013, 2015a). These models include Stark broadening profiles from Tremblay & Bergeron (2009), neutral line broadening, charged- and neutral-particle non-ideal effects from Hummer & Mihalas (1988), and H<sub>2</sub> molecular lines. The models also incorporate the Ly  $\alpha$  quasistatic single-perturber H–H<sub>2</sub> red-wing opacity of Kowalski & Saumon (2006) for  $T_{\text{eff}} \leq 9000$  K and the multi-perturber model Ly  $\alpha$  H–H and H–H<sup>+</sup> quasi-satellites via an updated version<sup>2</sup> of Allard & Kielkopf (2009) applied at  $T_{\text{eff}} > 9000$  K. The model spectra rely on the collision-induced absorption H<sub>2</sub>–H<sub>2</sub> opacity from Borysov et al. (2001) and the Hitran database<sup>3</sup>, including high-density corrections from Hare & Welsh (1958). These ingredients allow us to fit Ly  $\alpha$  and the continuum from UV-to-IR of pure-H atmosphere white dwarfs. The models with H<sub>2</sub> molecular lines switched on were only used when fitting the high-resolution COS spectra. Prior to fitting, the models were convolved with the appropriate line spread function for the required STIS or COS grating<sup>4</sup>, using the LINETOOLS PYTHON package<sup>5</sup>.

Kowalski (2026) recently identified the potential overabundance of the H<sub>3</sub><sup>+</sup> species in cool H-atmosphere models as a likely reason for the disagreement between models and *Gaia* data for white dwarfs cooler than 6000 K (Hollands et al. 2018b; Caron et al. 2023; O’Brien et al. 2024). Following the work of Kowalski (2026), it was realised that the H-atmosphere models had to be updated to remove the contribution of nuclear spin degeneracy to the H<sub>3</sub><sup>+</sup> partition function of Neale & Tennyson (1995) (S. Blouin private communication; see also Kilic et al. 2026)<sup>6</sup>, which had previously led to the overestimation of the partition function and abundance of H<sub>3</sub><sup>+</sup> in the models. We applied this correction to the models below 6000 K, resulting in a reduction of the H<sup>+</sup> opacity.

The grids of pure-H atmosphere model spectra span

<sup>1</sup> <https://warwick.ac.uk/fac/sci/physics/research/astro/people/tremblay/modelgrids/>

<sup>2</sup> <https://www.iap.fr/useriap/allard/lymantables.html>

<sup>3</sup> <http://hitran.org/cia/>

<sup>4</sup> <https://www.stsci.edu/hst/instrumentation/stis/performance/spectral-resolution>

<sup>5</sup> <https://github.com/linetools/linetools>

<sup>6</sup> The nuclear spin degeneracy is not included when considering partition functions of other hydrogen species, resulting in H<sub>3</sub><sup>+</sup> being treated inconsistently in previous models.

**Table 1.** Details of UV and optical spectroscopy available for 13 pc white dwarfs.

WD name	<i>HST</i> UV observation	<i>HST</i> UV PID	Optical observation or citation	Optical PID
0009+501	STIS G230L 52"×2"	14076	WHT/ISIS	–
0038–226	STIS G230L 52"×2"	14076	VLT/X-shooter	ESO 097.D–0064(A)
0046+051	STIS G230L 52"×2"	14076	VLT/X-shooter	ESO 098.D–0392(A)
0135–052	STIS G230L 52"×2"	14076	VLT/UVES	ESO 165.H–0588(A)
0141–675	STIS G230L 52"×2"	14076	VLT/X-shooter	ESO 099.D–0661(A)
0208–510	STIS G230L 52"×0.2"	14076	<i>HST</i> /STIS G430L 52"×0.2"	<i>HST</i> 12548
0245+541	STIS G230L 52"×2"	14076	Zuckerman et al. (2003)	–
0310–688	STIS E230M/E140M 0.2"×0.2"	14076	VLT/X-shooter	ESO 1103.D–0763(C)
0413–077	STIS E230M/E140M 0.2"×0.2"	14076	VLT/X-shooter	ESO 098.D–0392(A)
0426+588	STIS G230L 52"×0.5"; COS G140L	14076	Bergeron et al. (1997)	–
0435–088	STIS G230L 52"×2"	14076	VLT/X-shooter	ESO 098.D–0392(A)
0548–001	STIS G230L 52"×2"	14076	VLT/X-shooter	ESO 099.D–0661(A)
0552–041	STIS G230L 52"×2"	14076	VLT/X-shooter	ESO 098.D–0392(A)
0553+053	STIS G230L 52"×2"	14076	VLT/X-shooter	ESO 098.D–0392(A)
0642–166	STIS E230H/E140H 0.2"×0.09"	12981	<i>HST</i> /STIS G430L/G750M 52"×2"	<i>HST</i> 12606
0727+482 A	STIS G230L 52"×2"	14076	Bergeron et al. (2001)	–
0727+482 B	STIS G230L 52"×2"	14076	Bergeron et al. (2001)	–
0736+053	STIS G230LB 52"×0.2"	7398	<i>HST</i> /STIS G430L 52"×2"	<i>HST</i> 7398
0738–172	FOS G270H	2593	Giammichele et al. (2012)	–
0752–676	STIS G230L 52"×2"	14076	VLT/X-shooter	ESO 098.D–0392(A)
0810–353	–	–	Bagnulo & Landstreet (2020)	–
0821–669	STIS G230L 52"×2"	14076	Subasavage et al. (2007)	–
0839–327	STIS G230L 52"×2"; COS G140L	14076	VLT/X-shooter	ESO 098.D–0392(A)
0912+536	STIS G230L 52"×2"; COS G140L	14076	Bergeron et al. (1997)	–
1055–072	STIS G230L 52"×2"	14076	VLT/X-shooter	ESO 1103.D–0763(C)
1132–325	STIS G230L 52"×0.5"	14076	Giammichele et al. (2012)	–
1142–645	STIS G230L 52"×2"; COS G140L	14076	VLT/X-shooter	ESO 099.D–0661(A)
1202–232	STIS G230L 52"×2"; COS G140L	14076	VLT/X-shooter	ESO 098.D–0392(A)
1334+039	STIS G230L 52"×2"	14076	VLT/X-shooter	ESO 099.D–0661(A)
1345+238	STIS G230L 52"×2"	14076	Koester et al. (2001)	–
1620–391	STIS E230M/E140M 0.2"×0.2"	14076	VLT/UVES	ESO 167.D–0407(A)
1630+089	–	–	Limoges et al. (2013)	–
1647+591	COS G130M/G160M	14076	WHT/ISIS	–
1748+708	STIS G230L 52"×2"	14076	WHT/ISIS	–
1900+705	STIS G230L 52"×2"; COS G140L	14076	WHT/ISIS	–
1917–077	STIS E230M 0.2"×0.2"; COS G130M/G160M	14076	VLT/X-shooter	ESO 4109.A–0015(A)
1917+386	STIS G230L 52"×2"	14076	WHT/ISIS	–
1953–011	STIS G230L 52"×2"	14076	VLT/UVES	ESO 165.H–0588(A)
2140+207	STIS G230L 52"×2"; COS G140L	14076	VLT/UVES	ESO 097.D–0063(A)
2150+591	–	–	Tremblay et al. (2020)	–
2251–070	–	–	VLT/X-shooter	ESO 098.D–0392(A)
2359–434	STIS G230L 52"×2"	14076	VLT/X-shooter	ESO 099.D–0661(A)
G 203-47 B	STIS G230L 52"×2"	17778	–	–

$T_{\text{eff}} = 1500 - 40\,000$  K, and  $\log g = 7.0 - 9.0$  in steps of 0.5 dex. LTE models are appropriate for fitting the white dwarfs in this sample because they are well below 40 000 K, and non-LTE effects only become significant above that temperature, or in line cores at high-resolution. For the mass-radius relation, we used the thick H-layer option from Bédard et al. (2020),  $q_{\text{H}} = M_{\text{H}}/M_{\text{WD}} = 10^{-4}$ .

For the hybrid fitting of DA white dwarfs, we expanded on the fitting routine presented in Sahu et al. (2023). Briefly, the STIS spectra and photometry were combined, then compared to pure-H model spectra using the reduced  $\chi^2$  metric, and then the data were fitted using the least-squares method. Filter response functions and zeropoint fluxes for fitting photometry were taken from the Spanish Virtual Observatory (SVO) Filter Profile Service (Rodrigo et al. 2012; Rodrigo & Solano 2020). The SVO zeropoints were derived

using `alpha_lyr_stis_010.fits`<sup>7</sup> as the Vega reference spectrum for  $\lambda < 1\mu\text{m}$ , and `alpha_lyr_stis_011.fits`<sup>8</sup> for  $\lambda > 1\mu\text{m}$ .

Where multiple Balmer lines were visible in an optical spectrum, they were independently fitted using a `PYTHON` implementation that was created as part of the 4MOST white dwarf fitting pipeline `4MOST_WDPIPE`<sup>9</sup>. For these fits, we used pure-H 1D LTE models from Tremblay et al. (2011) (mixing length calibration of  $ML2/\alpha = 0.8$ ) with 3D corrections from Tremblay et al. (2013). In cool DA white dwarfs, hydrogen line broadening is increasingly dominated by

<sup>7</sup> [https://archive.stsci.edu/hlsps/reference-atlases/cdbs/calspec/alpha\\_lyr\\_stis\\_010.fits](https://archive.stsci.edu/hlsps/reference-atlases/cdbs/calspec/alpha_lyr_stis_010.fits)

<sup>8</sup> [https://archive.stsci.edu/hlsps/reference-atlases/cdbs/calspec/alpha\\_lyr\\_stis\\_011.fits](https://archive.stsci.edu/hlsps/reference-atlases/cdbs/calspec/alpha_lyr_stis_011.fits)

<sup>9</sup> [https://github.com/NPGFusillo/4MOST\\_WDpipe](https://github.com/NPGFusillo/4MOST_WDpipe)

**Table 2.** All spectroscopically confirmed white dwarfs within 13 pc of the Sun, listed in order of distance. Distances were determined using *Gaia* DR3 parallaxes of the white dwarfs or their companion stars in all cases, except for Procyon B which has a distance from van Leeuwen (2007). SpT refers to the spectral type. Comp. refers to the dominant atmosphere species.

WD name	Alternative name	SpT	Comp.	Distance (pc)
0642–166	Sirius B	DA	H	2.67
0736+053	Procyon B	DQZ	He	3.51
0046+051	van Maanen 2	DZA	He	4.31
1142–645	LAWD 37	DQ	He	4.64
0413–077	40 Eri B	DA	H	5.01
0426+588	Stein 2051 B	DC	He	5.52
1748+708	G 240-72	DXH	–	6.21
0552–041	LP 658-2	DZ	He	6.44
–	G 203-47 B	–	–	7.60
0553+053	G 99-47	DAH	H	8.12
0752–676	L 97-12	DA	H	8.17
2359–434	GJ 915	DAH	H	8.33
1334+039	Wolf 489	DA	H	8.35
2150+591	–	DAH	H	8.46
0839–327	GJ 318	DA	H	8.52
2251–070	LP 701-29	DZ	He	8.54
0038–226	LHS 1126	DQpec	He	9.10
0738–172	LAWD 25	DZA	He	9.15
0435–088	LHS 194	DQZ	He	9.40
1132–325	GJ 432 B	DZ	He	9.56
0141–675	L 88-59	DAZ	H	9.72
0912+536	G 195-19	DCH	He	10.27
0310–688	LB 3303	DAZ	H	10.40
1202–232	LP 852-7	DAZ	H	10.43
1917–077	LAWD 74	DBQA	He	10.51
0821–669	SCR 0821–6703	DA	H	10.68
0208–510	GJ 86 B	DQ	He	10.80
0245+541	LHS 1446	DAZ	H	10.87
0009+501	LHS 1038	DAH	H	10.87
1647+591	G 226-29	DAV	H	10.95
2140+207	LHS 3703	DQ	He	11.04
0810–353	–	DAH	H	11.17
0548–001	G 99-37	DQH	He	11.22
0727+482 A	G 107-70A	DA	H	11.27
0727+482 B	G 107-70B	DA	H	11.27
1953–011	LHS 3501	DAH	H	11.57
1345+238	LP 380-5	DC	H	11.86
1917+386	GJ 1234	DZ	He	11.87
1055–072	LHS 2333	DC	He	12.27
0135–052	L 870-2	DA+DA	H	12.62
1900+705	Grw+70°8247	DXH	–	12.88
1620–391	CD-38 10980	DAZ	H	12.91
1630+089	G 138-38	DA	H	12.93

neutral interactions, with resonance broadening as the main contributor, traditionally treated using the parameters of Ali & Griem (1965). Modelling dense, non-ideal plasmas is challenging, as volume effects from finite particle sizes can induce pressure ionisation. Most atmosphere codes adopt the Hummer–Mihalas occupation probability formalism, which treats atoms as hard spheres and removes states when interparticle distances fall below their radii (Hummer & Mihalas 1988). However, a straightforward application of this model yields systematically low  $\log g$  values below  $T_{\text{eff}} \lesssim 8000$  K, where neutral interactions dominate. To mitigate this, the hydrogen radius is reduced by a factor of two for the higher Balmer lines (Tremblay et al. 2010). We did not fit the Balmer lines and photometry simul-

taneously, as there is a well-known offset of  $\approx 2$  per cent between photometric and spectroscopic  $T_{\text{eff}}$  solutions for DA white dwarfs that is present when fitting different homogeneous spectroscopic and photometric data sets (Tremblay et al. 2019, 2020; Genest-Beaulieu & Bergeron 2019; Cukanovaite et al. 2021; Sahu et al. 2023; O’Brien et al. 2023).

For the confirmed unresolved double white dwarf system in the 13 pc sample, WD 0135–052, we fitted the Balmer lines from UVES spectra (Napiwotzki et al. 2020) to determine the parameters of both components of the system. We used the code `WD-BASS`<sup>10</sup> to fit the Balmer lines and photometry (Munday et al. 2024), where the same updated Tremblay et al. (2013, 2015a) models as discussed above were used for fitting. `WD-BASS` is a specialist code for fitting unresolved double white dwarf systems. It is standard to incorporate photometry from SDSS in fits with `WD-BASS` as well as *Gaia* photometry, and we removed the saturated SDSS  $u$  and  $z$  points prior to fitting. There were degeneracies in the fit due to the two white dwarfs having similar  $T_{\text{eff}}$ , so we restricted the  $T_{\text{eff}}$  bounds to remove the issue of stuck walkers in the MCMC.

We obtained the  $T_{\text{eff}}$  and  $\log g$  of the metal-enriched H-rich atmosphere white dwarfs (DAZ) using the hybrid fitting method described above, masking the metal lines during the fit as they are sufficiently narrow to not significantly impact the overall shape of the SED. Furthermore, metal abundances are low enough to have negligible influence on the equation-of-state and any hydrogen opacity including line broadening. Metal abundances were then derived using updated hydrogen-rich white dwarf atmosphere models based on the code of Koester (2010). Fixing the atmospheric parameters ( $T_{\text{eff}}$ ,  $\log g$ ) to the values obtained from the hybrid fit, the model grids were computed for each star over the abundance range  $-13 < \log(Z/H) < -6$  in steps of 0.2 dex. Calcium abundances were derived from the optical spectra by normalising the continuum in the region surrounding the Ca II K line and comparing the observed profiles with the model grid using a  $\chi^2$  minimisation technique. For carbon, oxygen, magnesium, and silicon, we used the flux-calibrated STIS spectra and performed fits in the wavelength regions encompassing the absorption features of each element as listed in Table 3. As with the hybrid fits to the DA white dwarfs, the synthetic spectra were convolved with the appropriate STIS line spread functions corresponding to the instrumental configuration of each observation, using the `LINETOOLS` python package. We then followed the methodology described in Williams et al. (2025) to model interstellar absorption simultaneously with the photospheric lines using the convolved spectra, thereby deriving the best-fitting elemental abundances and their corresponding uncertainties.

### 3.2 He-atmosphere fitting

Our analysis of helium-rich white dwarf spectra used models calculated with the code of D. Koester. The basic algorithms and atomic data are described in Koester (2010). The code and data have been updated continuously since then, with details occasionally described in the literature (Koester et al. 2014; Hollands et al. 2017; Gänsicke et al. 2018; Hollands et al. 2022; Elms et al. 2022). Here we summarise the most important changes to the code that are relevant for the cool, helium-rich white dwarfs in the 13 pc sample.

**Equation of state:** Deviations from the ideal gas law become noticeable at densities of  $0.01 \text{ g cm}^{-3}$ , and significant for values larger than  $0.1 \text{ g cm}^{-3}$ . The latter value is reached in the photosphere of pure-He

<sup>10</sup> <https://github.com/JamesMunday98/WD-BASS>

**Table 3.** List of lines used to derive the metal abundances for the DAZ white dwarfs within 13 pc. The lines marked by \* can have contributions of both photospheric and interstellar lines.

Ion	Vacuum wavelength [Å]
C II	1334.53*, 1335.66*, 1335.71*
C III	1174.93, 1175.26, 1175.59, 1175.71, 1175.98, 1176.37
O I	1152.15, 1302.17*, 1304.86*, 1306.03
Mg II	2796.35, 2803.53
Si II	1190.42*, 1193.29*, 1194.50, 1197.39, 1260.42*, 1264.74, 1265.00, 1304.37*, 1309.45
Si III	1294.54, 1296.72, 1298.89, 1301.15, 1303.32
Ca II	3933.66

white dwarfs with  $T_{\text{eff}} \approx 7500$  K, and for somewhat lower  $T_{\text{eff}}$  values if traces of elements with lower ionisation potentials (hydrogen or metals) are present. For these objects, non-ideal effects in the equation of state and absorption coefficients must be taken into account. Since a fully consistent treatment that can be applied to stellar atmosphere calculations is not available, simplifying approximations are used.

The most important quantity for the equation of state is the ionisation balance of helium, since it determines the  $\text{He}^-$  absorption coefficient. Kowalski et al. (2007) calculated this degree of ionisation as a function of density for two temperatures: 11 605 K (1 eV) and 5803 K (0.5 eV). Their calculations of the electron interaction energy, which is an important factor for determining the lowering of the ionisation potential, show that it is roughly linear with density (their Fig. 3) and exhibits only a weak temperature dependence at these specific temperatures (their Fig. 4). However, the overall ionisation balance and band gap become highly sensitive to temperature as it increases, particularly above 1.5 eV (their Fig. 7). At these higher temperatures, the atmospheric density is much lower. A correction term for the free energy can be constructed, which scales as  $\sim N^2/V$ , where  $N$  is the number of helium atoms and  $V$  is the volume. The change of the ionisation potential derived in the usual way from that correction term is thus linear in density. The constant in the relation was determined from a comparison with the result from Kowalski et al. (2007). With this procedure the ionisation balance from the code closely follows the result of the much more complicated calculation of Kowalski et al. (2007). Applying a correction term to the free energy enables the derivation of a consistent correction to pressure and the secondary quantities of specific heat and adiabatic gradient. The pressure correction becomes large when the density reaches above  $1 \text{ g cm}^{-3}$ , and is very similar to the calculations of Becker et al. (2014) (their Fig. 5). It should be noted that this treatment of the helium ionisation is similar to the so-called “excluded volume” model of the free energy.

Blouin et al. (2018) calculated the lowering of the ionisation potentials for five important metals: Na, Mg, Fe, Ca, and C. We used the equations from Blouin et al. (2018), which depend on density and weakly on temperature, for our calculations. For the calculation of line spectra the non-ideal changes to the occupation numbers of all states are important, which is treated with the occupation probability formalism of Hummer & Mihalas (1988). However, it is known that this formalism does not lead to pressure ionisation of hydrogen and helium (Mihalas et al. 1990), which therefore has to be treated separately as described above.

**Continuous absorption coefficients:** The most important continuous absorption coefficients in cool He-rich atmosphere white dwarfs are the free-free absorption of  $\text{He}^-$  and He Rayleigh scattering.

High-density corrections for  $\text{He}^-$  have been determined by Iglesias et al. (2002), and were recalculated by S. Blouin (priv. comm.). The high-density Rayleigh scattering coefficients are from Rohrmann (2018). At low temperatures in He-rich models, CIA becomes important. Incorporated in the models are He– $\text{H}_2$  (Abel et al. 2012) and He–He–He (Kowalski 2014). If the abundance of metals is large (e.g. in DQs), the photoabsorption cross sections from TOPBASE are included (Seaton 1995).

**Spectral line absorption:** At high densities, many spectral lines show broad profiles with asymmetries, and sometimes “satellites” on their wings that are not consistent with the classical Voigt profiles of the absorption coefficients. These lines are analysed with “unified theories” that aim to describe the core as well as the far wings of the lines, including possible satellites. The theory was developed by Allard & Kielkopf (1982); Allard et al. (1999). The D. Koester code uses an independent method with improved numerical algorithms. Such line profiles are now available for Ly  $\alpha$  (broadened by H,  $\text{H}^+$ ,  $\text{H}_2$ , He), Ly  $\beta$  (H,  $\text{H}^+$ ), Ly  $\gamma$  (H,  $\text{H}^+$ ), C I 1657, 1931, 2479, Na I 5892, 5898, Mg I 2853, 5169, 5174, 5185, Mg II 2796, 2804, Ca I 4228, and Ca II 3935, 3870 Å.

The line lists of the  $\text{C}_2$  and CH bands from the ExoMOL database (Tennyson et al. 2016, 2024) have been implemented in the code for DQ white dwarfs. Using the “Just Overlapping Line” formulation, as developed in Zeidler-K. T. & Koester (1982) gives almost identical results with much less computational effort, so that formulation was used for  $\text{C}_2$  in the code. The shift of the electronic energy levels, that causes the shift of the Swan bands in the DQpec stars, was found by quantum mechanical simulations to be  $\delta E = 1.8\rho$  (Kowalski 2010). However, Kowalski (2010); Blouin et al. (2019c) changed the constant to 0.2, for better fits to the observations, and in some cases a value of 0.1 gives the best fits. As noted by Blouin et al. (2019c), no single value of this constant fits all objects. These problems are also related to uncertainties in helium ionisation equilibrium and hydrogen abundance (Kowalski 2010).

### 3.2.1 DC fitting

We fitted three DC white dwarfs with a similar hybrid fitting method as described in Section 3.1. He-atmosphere models with trace hydrogen were generated using the code of Koester (2010). The He + H grids of model spectra span  $T_{\text{eff}} = 3000 - 20\,000$  K in steps of 250 K,  $\log g = 7.0 - 9.5$  in steps of 0.25 dex, and  $\log(\text{H}/\text{He}) = -6.0$  to 0.0 (plus pure-He) in steps of 0.25 dex. We chose to apply He + H models to fit the combined STIS spectra and photometry of the featureless DC white dwarfs, WD 0426+588, WD 1055–072, and WD 0912+536, as their  $T_{\text{eff}}$  values are high enough that Balmer lines would be detectable in the spectra if they had pure-H atmospheres. We applied a reduced  $\chi^2$  least-squares fit to the STIS spectra and photometry, to determine  $T_{\text{eff}}$  and  $\log g$ . For the mass-radius relation, we used the thin H-layer option from Bédard et al. (2020),  $q_{\text{H}} = 10^{-10}$ . Since hydrogen is an additional free parameter in the model spectra, we interpolated over the grids to find the best solution or upper limit for  $\log(\text{H}/\text{He})$  as well as  $T_{\text{eff}}$  and  $\log g$ . Once the initial fit was complete, we generated grids of models incorporating varying levels of trace carbon, and all other parameters fixed, to determine upper limits on the carbon abundances.

### 3.2.2 DQ fitting

To fit the DQ white dwarfs, He-atmosphere models with carbon were generated using the code of Koester (2010). The He + C grids

of model spectra span  $T_{\text{eff}} = 3000 - 12\,000$  K in steps of 250 K,  $\log g = 7.25 - 9.75$  in steps of 0.25 dex, and  $\log(C/\text{He}) = -3.0$  to  $-9.5$  in steps of 0.5 dex. Some specific objects required tailored grids with hydrogen or metals included, which are discussed further in Section 4.2.2.

In the STIS spectra, the strong neutral atomic carbon lines, C I 1657 Å, 1930 Å and 2478 Å, are substantially weaker than predicted with models, given the fits to the optical Swan bands, with the C I 2478 Å line being especially problematic. Provencal et al. (2002) found that the best fit to the UV C I lines for Procyon B was a factor of  $\sim 30$  lower than the abundance from the optical Swan band fit. The fact that UV carbon features are stronger in models than in spectroscopic data has also been noted previously by Dufour (2011); Coutu et al. (2019); Koester & Kepler (2019), and seems to be universal for DQs. While this discrepancy has historically been attributed to the inadequacy of the classical van der Waals broadening treatment within the impact approximation, we used models with updated unified C I line profiles. Because this discrepancy was not improved with the addition of unified profiles, we artificially decreased the  $gf$  values in the models. The  $gf$  parameter corresponds to the oscillator strengths of transitions between two energy levels. Following this adjustment, the predicted line strengths from the models were similar to those observed for C I 1657 Å, 1930 Å and 2478 Å.

We adopted a fitting method for DQs that has been used for many decades (Bergeron et al. 1997; Dufour et al. 2005; Blouin & Dufour 2019; Coutu et al. 2019). In brief, the photometry and spectral features are fitted independently to constrain the three free parameters,  $T_{\text{eff}}$ ,  $\log g$ , and  $\log(C/\text{He})$ . The main difference between our method and previous studies is the inclusion of the STIS spectra in the photometric part of the fit. Our procedure was as follows: we fixed the models to a starting  $\log(C/\text{He})$ , and performed a hybrid fit to the STIS spectrum plus the optical and IR photometry. We determined  $T_{\text{eff}}$  and  $\log g$  from a fit to the STIS spectrum plus photometry. Then, we fixed the  $T_{\text{eff}}$  and  $\log g$  from the initial fit, and fitted the carbon lines in the optical spectrum to determine  $\log(C/\text{He})$ . We generated new models with the new  $\log(C/\text{He})$  and again fitted the spectrophotometric data to determine  $T_{\text{eff}}$  and  $\log g$ . We repeated these steps until convergence, while additionally varying  $\log(H/\text{He})$  until the lowest reduced  $\chi^2$  was reached, in order to determine limits on hydrogen for all objects. We did not attempt to fit the UV carbon lines to determine abundances due to the issues mentioned above with the line strengths of UV carbon.

DQpec white dwarfs are a subset of the DQ class, in which the central wavelengths of the Swan bands are shifted bluewards by 100–300 Å from their typical positions (Hall & Maxwell 2008). Using quantum-mechanical simulations, Kowalski (2010) determined a shift of the electronic levels, and thus the Swan bands, that could be described as  $d(\text{eV}) = a \cdot \rho(g \text{ cm}^{-3})$ , with  $a = 1.6$ . However, this value results in a distortion that is much stronger than observed, forcing Kowalski (2010) and Blouin & Dufour (2019) to use an empirical calibration to get a best value of  $a = 0.2$ . These studies noted that no single value gives a good fit for all DQpec. The problem is connected with the uncertainty in ionisation equilibrium of helium and hydrogen content in the extreme atmospheres of these stars. For the fits in this work, we tested the impact of the parameter  $a$  on our objects and other DQ white dwarfs, and settled on  $a = 0.1$  for the model grids.

### 3.2.3 DZ fitting

Fitting of cool, metal-enriched helium-atmosphere white dwarfs (DZ) requires bespoke model atmosphere grids for each object. The

models generated for our fits were from the code of Koester (2010). Our models include several features required for the analysis of DZ white dwarfs, namely calculations for unified line profiles of the Ca II H and K doublet, Ca I 4227 Å, Mg II H and K doublet, Mg I b triplet, Mg I 2853 Å, and Na D doublet, as described in Hollands et al. (2017, 2022). For the DZ spectra, we used the same iterative fitting procedure as for the DQ white dwarfs, explained in Section 3.2.2. Due to the low  $T_{\text{eff}}$  of some of these DZ stars, the metal features could not be fitted independently, as abundances of metals were correlated, and changing one metal abundance affected the shape of other metal lines. In the models we included some metals that are not detected in the spectra but are major rock forming elements (such as silicon and nickel). We fixed the abundances of these undetected elements relative to calcium by assuming ratios of bulk Earth composition. The details of the models used for each individual DZ are discussed in Section 4.2.4.

## 4 RESULTS

### 4.1 H-atmosphere results

The best-fitting parameters for the H-atmosphere 13 pc white dwarfs, determined using the fitting methods outlined in Section 3, are presented in Table 4. We fitted STIS spectra alongside *Gaia* DR3  $G$ ,  $G_{\text{BP}}$ ,  $G_{\text{RP}}$ ; 2MASS  $J$ ,  $H$ ,  $K_s$ ; and WISE  $W1$ ,  $W2$  photometry, where available, in a hybrid fit. We fitted the data with two different approaches for most white dwarfs: once including the STIS spectrum, labelled as ‘with UV’, and once without it, labelled as ‘without UV’ in Table 4. Additional independent parameters determined from fits to the Balmer lines of DA white dwarfs are also presented in Table 4.

#### 4.1.1 Hybrid fits

Figures 2 and 3 show the best-fit models for two different fits of H-atmosphere white dwarfs: one including STIS spectra plus optical and IR photometry (blue models), and another for just optical and IR photometry (red models). Low-resolution *Gaia* XP spectra are also displayed in Figs. 2 and 3. *Gaia* XP spectra provide a visual insight into the performance of the models, but their flux calibration has not been validated as extensively across data releases and external surveys (see, e.g. Elms et al. 2024) as *Gaia* photometry. Since the photometry itself is partly derived from XP spectra, we chose to fit the *Gaia* photometry instead and consequently the XP spectra were not incorporated into the hybrid fit. For plotting the XP spectra, we applied the corrections derived by Huang et al. (2024), who used CALSPEC and LAMOST data. In all plots, the XP spectra were cropped at the blue end to remove noise. Figure 2 shows fits to the flux-calibrated, low-resolution STIS G230L spectra, and Fig. 3 shows fits to the high-resolution STIS E140M spectra. For some of the coolest spectra, the fits with and without STIS show significant overlap in Fig 2, as the STIS flux is minimal and does not significantly affect the overall fit to the SED.

For WD 0642–166 (Sirius B), all photometry was at least partially contaminated, so the fits presented in Fig. 3 are to the G430L spectrum plus the suboptimally flux-calibrated STIS E140H spectrum scaled to the flux-calibrated G430L spectrum (blue), and the G430L spectrum independently (red). Our mass of Sirius B from the STIS G430L fit is  $1.022 M_{\odot}$ , and we also determine a mass of  $1.069 M_{\odot}$  from fits to Balmer lines. Bond et al. (2017a) determined an astrometric mass of  $1.018 \pm 0.011 M_{\odot}$  for Sirius B using *HST*, which is independent from atmosphere models. Bond et al. (2017b) calculated an

**Table 4.** Best-fit parameters for H-atmosphere white dwarfs within 13 pc of the Sun. A fit with UV refers to hybrid spectrophotometric parameters for white dwarfs observed with *HST* STIS or COS. Symbols indicate the photometry used for the fit. No symbol indicates *Gaia*, 2MASS and WISE. \* indicates *Gaia* and 2MASS. ‡ indicates *BVRI* + 2MASS photometry. § indicates STIS G430L was used in the fit. Any metal features were masked for these fits. Uncertainties are purely statistical. Masses were determined with UV, unless UV data was not available or only high-resolution UV spectra were used.

WD name	SpT	$T_{\text{eff}}$ (K) (with UV)	$\log g$ (with UV)	$T_{\text{eff}}$ (K) (without UV)	$\log g$ (without UV)	Mass ( $M_{\odot}$ )	$T_{\text{eff}}$ (K) (Balmer)	$\log g$ (Balmer)
0009+501	DAH	6837 ± 6	8.365 ± 0.004	6674 ± 42	8.313 ± 0.016	0.825 ± 0.003	6529 ± 62	8.35 ± 0.08
0141–675	DAZ	6705 ± 3	8.145 ± 0.003	6444 ± 25	8.021 ± 0.010	0.680 ± 0.002	6410 ± 4	7.859 ± 0.006
0245+541	DAZ	5211 ± 4	8.224 ± 0.003	5115 ± 19	8.167 ± 0.013	0.724 ± 0.002	–	–
0310–688	DAZ	15 714 ± 5	8.041 ± 0.001	16 449 ± 158	8.135 ± 0.011	0.696 ± 0.007	16 205 ± 12	8.12 ± 0.003
0413–077 *	DA	16 333 ± 6	7.900 ± 0.001	16 697 ± 339	7.964 ± 0.026	0.596 ± 0.015	16 959 ± 10	7.981 ± 0.002
0553+053	DAH	6112 ± 3	8.346 ± 0.004	5827 ± 32	8.213 ± 0.014	0.811 ± 0.003	–	–
0642–166 §	DA	25 199 ± 4	8.60 ± 0.3	25 527 ± 33	8.640 ± 0.016	1.022 ± 0.009	25 762 ± 106	8.723 ± 0.025
0727+482 A ‡	DA	5015 ± 17	7.839 ± 0.064	4966 ± 87	7.941 ± 0.061	0.544 ± 0.036	–	–
0727+482 B ‡	DA	5064 ± 70	8.17 ± 0.14	4979 ± 106	8.162 ± 0.067	0.682 ± 0.044	–	–
0752–676	DA	5754 ± 1	8.034 ± 0.002	5687 ± 10	8.001 ± 0.006	0.607 ± 0.001	5634 ± 199	7.986 ± 0.011
0810–353	DAH	–	–	6503 ± 43	8.285 ± 0.020	0.771 ± 0.013	–	–
0821–669	DA	5079 ± 5	8.142 ± 0.004	4960 ± 26	8.061 ± 0.017	0.670 ± 0.003	–	–
0839–327	DA	9527 ± 4	7.931 ± 0.002	9196 ± 36	7.815 ± 0.009	0.559 ± 0.001	9227 ± 9	7.786 ± 0.046
1202–232	DAZ	8973 ± 8	8.128 ± 0.003	8539 ± 75	7.972 ± 0.022	0.675 ± 0.002	8637 ± 4	7.911 ± 0.006
1334+039	DA	5101 ± 3	8.035 ± 0.003	5011 ± 15	7.969 ± 0.012	0.602 ± 0.002	–	–
1345+238	DC	4797 ± 7	7.964 ± 0.006	4725 ± 39	7.910 ± 0.028	0.557 ± 0.004	–	–
1620–391	DAZ	23 238 ± 25	7.935 ± 0.003	25 011 ± 527	8.071 ± 0.032	0.675 ± 0.020	24 651 ± 26	8.2 ± 0.1
1630+089	DA	–	–	5664 ± 9	8.075 ± 0.006	0.632 ± 0.004	5571 ± 76	7.926 ± 0.016
1647+591	DAV	12 408 ± 17	8.32 ± 0.02	12 240 ± 107	8.304 ± 0.012	0.796 ± 0.008	12 283 ± 35	8.324 ± 0.009
1953–011	DAH	8382 ± 8	8.400 ± 0.004	8000 ± 69	8.242 ± 0.020	0.852 ± 0.003	7688 ± 28	8.2 ± 0.1
2150+591 *	DAH	–	–	5244 ± 33	8.103 ± 0.021	0.646 ± 0.014	–	–
2359–434	DAH	8941 ± 7	8.530 ± 0.003	8683 ± 70	8.429 ± 0.016	0.937 ± 0.002	8383 ± 5	8.265 ± 0.005

astrometric mass for WD 0413–077 (40 Eri B) of  $0.573 \pm 0.018 M_{\odot}$ , compared to our values of  $0.560 M_{\odot}$  (with UV),  $0.596 M_{\odot}$  (without UV), and  $0.606 M_{\odot}$  (Balmer fit).

Photometric fits to the components of the resolved binary WD 0727+482 A+B are shown in Fig. 4. These two white dwarfs are part of a quadruple star system with a pair of M dwarfs, and we take the *Gaia* parallax of these M dwarfs to be equivalent to those of WD 0727+482 A+B in Table 2, as the white dwarfs do not have *Gaia* parallaxes. The white dwarfs also have no *Gaia* photometry, but Bergeron et al. (2001) observed the system in *BVRI* bands, which we incorporated into the fits.

Three 13 pc H-atmosphere white dwarfs, WD 0810–353, WD 1630+089 and WD 2150+591, did not have STIS spectra available, so we fitted just their photometry in Fig. 5. For WD 2150+591, there is a 2MASS *J*-magnitude excess above the model in Fig. 5, which we believe is caused by contamination from a nearby bright star. The DAV WD 1647+591 was not observed with STIS so we instead applied a hybrid fitting method with the COS spectrum and photometry in Fig. 6. This white dwarf shows many molecular H<sub>2</sub> lines in its high-resolution COS spectrum that were implemented in our models.

#### 4.1.2 Fits to Balmer lines

Fits to the Balmer lines of DA white dwarfs from optical spectroscopy are shown in Fig. 7. The wings of the lines fit well in all cases, but the cores of the lines in some stars are not well-modelled, possibly due to neglecting non-LTE effects and 3D overshoot (Tremblay et al. 2013). However, this generally has a small effect on the resulting best fit parameters, with possible differences also due to data flux calibration or Zeeman splitting of the line cores. These fits provide an extra set of parameters for single DA white dwarfs in Table 4. There

are known discrepancies between photometric and spectroscopic fits of DA white dwarfs, see O’Brien et al. (2023) for details.

In Table 5, we provide the best-fit parameters for both components of the well-known double-lined double degenerate system WD 0135–052 (Saffer et al. 1988), from the fit to each of the two UVES spectra plus photometry. We fitted this system using the *wd-bass* code (Munday et al. 2024). The fits to the Balmer lines of WD 0135–052 are shown in Fig. 8, where we also show the two models that combined to fit the spectrum observed at epoch HJD 51741.8696, compared to the full SED of WD 0135–052. The error bars on the parameters are large due to the two white dwarfs having a similar  $T_{\text{eff}}$ , which has introduced degeneracies into the fit.

#### 4.1.3 Fits to photospheric metal lines

The metal abundances from fits to DAZ white dwarfs are presented in Table 6. WD 0141–675 and WD 1202–232 display only calcium lines in the optical and no photospheric lines in the UV. WD 0310–688 and WD 1620–391 appear to be pure-H atmosphere DAs in the optical, but display many photospheric metal lines in the UV. We did not have access to any Ca II H and K line coverage of the DAZ white dwarf WD 0245+541, however Zuckerman et al. (2003) measured the calcium abundance of this star to be  $\log(\text{Ca}/\text{H}) = -12.7$  using a Keck HIRES spectrum.

None of the DAZ white dwarfs in our sample have metal lines newly-identified from this work. WD 0141–675 has been well-studied, as it has a now-retracted astrometric planet candidate from *Gaia* DR3 (Rogers et al. 2024; Ramírez et al. 2025). (Rogers et al. 2024) found similar issues for WD 0141–675, finding that the optical fits under-predicted the STIS spectrum flux. Zuckerman et al. (2003) measured the calcium abundance of WD 1202–232. WD 0310–688 was previously reported to show a mid-IR excess from *JWST* MIRI,

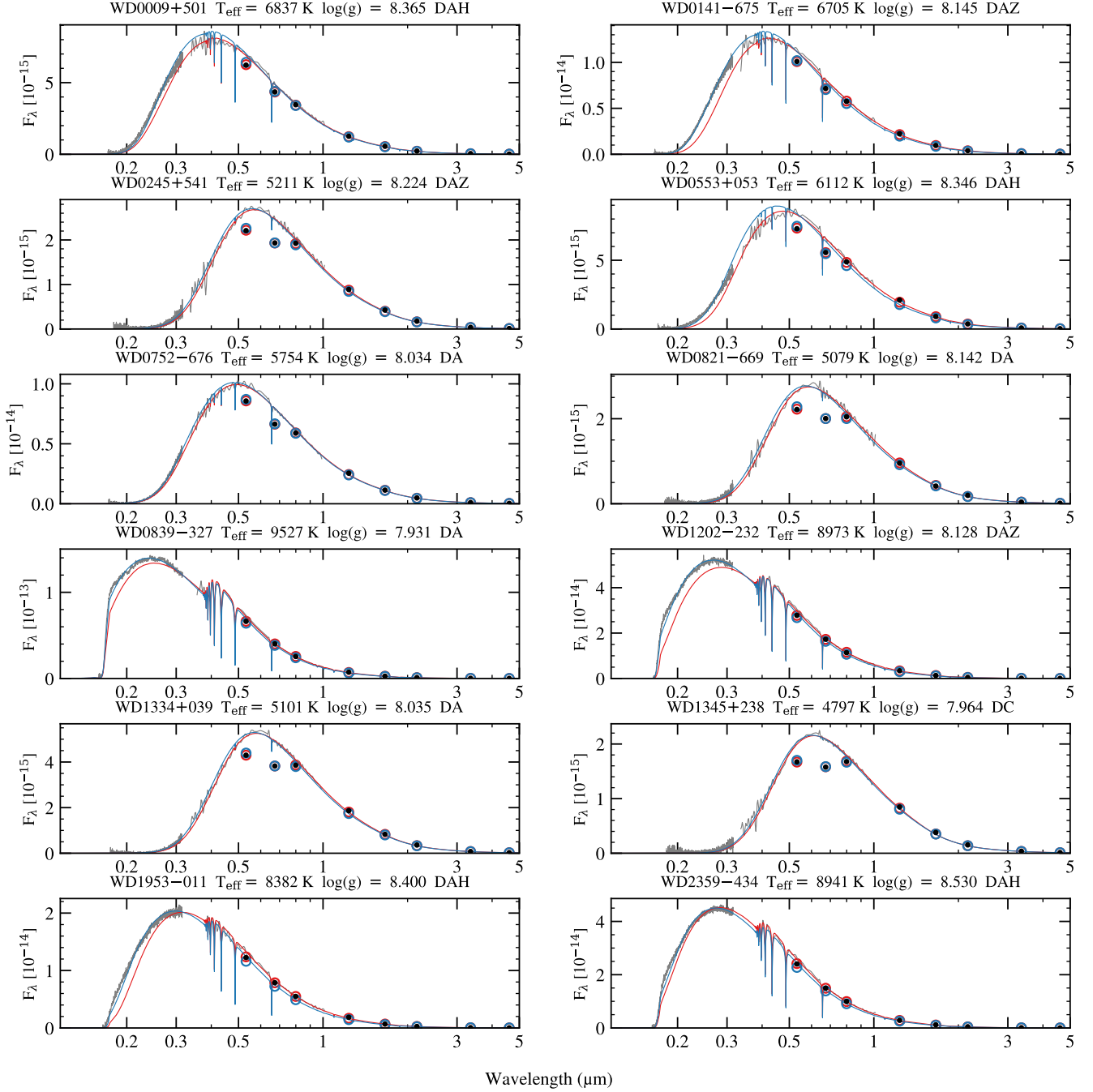


**Figure 2.** Hybrid spectrophotometric fits of H-atmosphere white dwarfs in the 13 pc sample with flux-calibrated STIS G230L spectra. Flux is given in units of  $\text{erg cm}^{-2} \text{s}^{-1} \text{\AA}^{-1}$ . The blue models are best fits to STIS spectra plus *Gaia*, 2MASS, and WISE photometry plus parallaxes, where available. The red models are the fits to just the *Gaia*, 2MASS, and WISE photometry plus parallaxes. All parameters in this figure are from the fits to STIS plus photometry (blue models). *Gaia* XP spectra are shown but not incorporated into the fits.

due to a giant planet candidate or cold debris disk (Limbach et al. 2024); the same STIS spectrum discussed in their work is analysed and fitted here. The STIS spectrum of WD 1620–391 analysed in this work was also analysed by Debes et al. (2025) who did not find an infrared excess for this object using *JWST* MIRI.

## 4.2 He-atmosphere results

### 4.2.1 DC results

Figure 10 shows the best fits to the DC white dwarfs with He-rich atmospheres in 13 pc, with fits to the STIS spectra plus optical and IR photometry shown in red. Table 7 lists the best-fitting parameters for the DC white dwarfs. We found that the best-fitting models to just

**Table 5.** Parameters from combined spectroscopic and photometric fits to the double lined system WD 0135–052. UVES spectra of the two epochs were fitted individually.

Observation HJD [days]	$T_{\text{eff},1}$ (K) (Balmer)	$\log g_1$ (Balmer)	$T_{\text{eff},2}$ (K) (Balmer)	$\log g_2$ (Balmer)
51737.8611	$7504^{+126}_{-125}$	$8.056^{+0.040}_{-0.083}$	$7243^{+51}_{-87}$	$7.701^{+0.030}_{-0.026}$
51741.8696	$7403^{+72}_{-57}$	$7.755^{+0.025}_{-0.026}$	$7080^{+88}_{-170}$	$7.917^{+0.056}_{-0.035}$

**Table 6.** Photospheric metal abundances of hydrogen-atmosphere white dwarfs within 13 pc of the Sun.  $T_{\text{eff}}$  and  $\log g$  for these stars are listed in Table 4.

WD name	SpT	$\log(\text{Ca}/\text{H})$	$\log(\text{Mg}/\text{H})$	$\log(\text{O}/\text{H})$	$\log(\text{Si}/\text{H})$	$\log(\text{C}/\text{H})$
0141–675	DAZ	$-10.7 \pm 0.02$	–	–	–	–
0310–688	DAZ	–	$-7.77 \pm 0.09$	$-7.14 \pm 0.12$	$-7.93 \pm 0.06$	–
1202–232	DAZ	$-9.7 \pm 0.01$	–	–	–	–
1620–391	DAZ	–	–	–	$-7.41 \pm 0.15$	$-7.73 \pm 0.08$

the optical and IR photometry do not reliably predict the UV flux, and therefore we did not include parameters for fits without STIS in Table 7. The H + He DC models are sensitive to the Ly  $\alpha$  opacity, especially in the UV, which makes them responsive to the presence of trace hydrogen, and therefore adding the STIS spectra to our fits enabled us to constrain the hydrogen content.

WD 0426+588 and WD 1055–072 required hydrogen for a good fit. WD 0426+588 has a model-independent mass measurement of  $0.675 \pm 0.051 M_{\odot}$  determined from microlensing (Sahu et al. 2017). Our mass from UV fitting is  $0.594 M_{\odot}$ , which is within  $2\sigma$  of the microlensing mass. The magnetic DCH WD 0912+536, with a 100 MG field strength (Angel et al. 1972; Bagnulo & Landstreet 2020), fitted well with pure-He models. The magnetic field was identified with continuum polarisation measurements, and the strong field does not alter the shape of the SED due to a lack of spectral features.

We tested the effects of adding carbon rather than hydrogen to the DC models, as trace carbon is known to reproduce UV cooling tracks (Blouin et al. 2023; Camisassa et al. 2023). Helium and trace carbon models were tested on the two DCs that fitted well with  $\log(\text{H}/\text{He}) \approx -5$ , WD 0426+588 and WD 1055–072, and they produced substantially worse fits. We then generated C + H + He models with  $T_{\text{eff}}$ ,  $\log g$ , and  $\log(\text{H}/\text{He})$  fixed at their best-fitting values from the fits with H + He models, and  $\log(\text{C}/\text{He})$  as the only free parameter. Fitting with these models provided an upper limit for the carbon content:  $\log(\text{C}/\text{He}) = -8.4$  for WD 0426+588, and  $\log(\text{C}/\text{He}) = -9.0$  for WD 1055–072. These limits are discussed in the context of DQs in Section 5.2.

#### 4.2.2 DQ results

The best-fitting parameters and abundances for the DQ white dwarfs within 13 pc are presented in Table 8 and fits are shown Fig. 11. Each DQ white dwarf required tailored modelling, and we discuss them individually below.

**WD 0038–226:** For fitting this DQpec, we used the standard DQ models to fit the full SED including STIS, and then shifted the models by  $100 \text{ \AA}$  to fit the Swan bands and obtain  $\log(\text{C}/\text{He})$ . This star has the weakest carbon abundance of any known DQ white dwarf. Blouin & Dufour (2019) fitted an optical spectrum of WD 0038–226 and determined a  $\log(\text{C}/\text{He})$  of  $-8.4$ , which is 0.5 dex higher than the abundance determined in this work. This discrepancy is possibly due to the differences in the models used to fit these white dwarfs, as WD 0038–226 displays CIA (Giammichele et al. 2012), the ef-

fects of which are challenging to model. Blouin et al. (2024) derived an independent mass– $T_{\text{eff}}$  relation for WD 0038–226, and our solution of 5600 K and  $0.65 M_{\odot}$  agrees with this relation. The shape of the UV flux of WD 0038–226 fitted better with trace hydrogen added to the models at  $\log(\text{H}/\text{He}) = -6.5$ . Wolff et al. (2002) observed WD 0038–226 with the *HST*/FOS in the UV, and also found that a low hydrogen abundance provided a better fit compared with zero hydrogen. However, any amount of hydrogen greatly suppresses the strength of the Swan bands compared to the observations, and none of our models could fit the Swan bands as well as a hydrogen-free model did. Additionally, Blouin et al. (2024) found that for WD 0038–226,  $\log(\text{H}/\text{He}) > -5$  would produce a  $2.4 \mu\text{m}$  feature which they did not detect with *JWST*. Therefore, we elected not to include hydrogen in our final fit to WD 0038–226.

**WD 0208–510:** This DQ is in a close binary with a K dwarf companion, making optical spectroscopic observations challenging. Farihi et al. (2013) obtained *HST* data of this star, and fitted the combination of STIS optical G430L spectra plus UV and optical photometric Wide Field Camera 3 (WFC3) UVIS points, and determined a  $\log g$  of 8.02 and  $\log(\text{C}/\text{He})$  of  $-4.8$ . Our fits to the STIS UV G230L spectra without photometry produced a much lower  $\log g$  of 7.574, and a lower  $\log(\text{C}/\text{He})$  of  $-5.81$ . In an attempt to reconcile this difference, we fixed the  $\log g$  to 8 and fitted for  $T_{\text{eff}}$  and  $\log(\text{C}/\text{He})$ . We were unable to obtain a satisfactory fit to both the UV spectrum and the optical Swan bands. The  $\log(\text{C}/\text{He})$  determined by Farihi et al. (2013) provided a good fit to the overall SED but the Swan bands were much weaker and required a  $\log(\text{C}/\text{He})$  of 1 dex lower to fit well with our models. Therefore, we decided to present the parameters determined in our initial fit, keeping the low  $\log g$  rather than fixing  $\log g$  to 8.

**WD 0435–088:** We observed a weak Mg II feature at  $2800 \text{ \AA}$  in the STIS G230L spectrum of this white dwarf, which is shown in an inset plot in Fig. 11. We therefore recomputed models with low levels of magnesium, with all other parameters kept constant in the models. This is the first detection of photospheric metals in the atmosphere of this DQ white dwarf, adding to the small number of known DQZ white dwarfs alongside WD 0736+053 (Procyon B).

**WD 0548–001:** To fit this DQH white dwarf with CH molecular bands, we generated a small grid covering  $T_{\text{eff}} = 5500 - 6500 \text{ K}$  in steps of 250 K,  $\log g = 7.75 - 8.50$  in steps of 0.25 dex,  $\log(\text{C}/\text{He}) = -5.5$  to  $-6.5$  in steps of 0.25 dex, and  $\log(\text{H}/\text{He}) = -5.5$  to  $-6.5$  in steps of 0.25 dex. This white dwarf has a magnetic field strength of 7 MG (Bagnulo & Landstreet 2022), which affects the

**Table 7.** Best-fit parameters for He-rich DC white dwarfs within 13 pc of the Sun. The  $T_{\text{eff}}$  and  $\log g$  are hybrid spectrophotometric parameters determined from fitting STIS spectra plus optical and IR photometry. Symbols indicate the photometry used for the fit. No symbol indicates *Gaia*, 2MASS and WISE. \* indicates *Gaia* and 2MASS/JHK photometry.

WD name	SpT	$T_{\text{eff}}$ (K)	$\log g$	Mass ( $M_{\odot}$ )	$\log(\text{H/He})$
0426+588 *	DC	$6828 \pm 2$	$8.033 \pm 0.002$	$0.594 \pm 0.001$	$-5.4 \pm 0.5$
0912+536	DCH	$7579 \pm 3$	$8.399 \pm 0.002$	$0.834 \pm 0.001$	pure He
1055-072	DC	$6540 \pm 3$	$8.068 \pm 0.004$	$0.615 \pm 0.002$	$-4.9 \pm 0.5$

shape of the molecular features in the optical and UV spectra. We fitted the spectra of WD 0548–001 with non-magnetic models and achieved an acceptable fit. However, the fit to the CH molecular feature near 4300 Å is sub-optimal.

**WD 0736+053:** To fit WD 0736+053 (Procyon B), we used a grid with fixed  $\log g$  and metal abundances (magnesium, iron, calcium), with  $T_{\text{eff}}$ ,  $\log(\text{C/He})$  and  $\log(\text{H/He})$  allowed to vary. We chose to fix some parameters in the models due to the number of free parameters being so large. The DQZ grid spans  $T_{\text{eff}} = 7250 - 8250$  K in steps of 250 K,  $\log(\text{C/He}) = -5.0$  to  $-6.0$  in steps of 0.25 dex, and  $\log(\text{H/He}) = -4.0$  to  $-5.0$  in steps of 0.5 dex. The  $\log g$  in the models was fixed at 8.03, derived from a dynamical mass of Procyon B determined by Bond et al. (2015). The metal abundances in the grid were fixed at the values determined by Provencal et al. (2002):  $\log(\text{Mg/He}) = -10.5$ ,  $\log(\text{Fe/He}) = -10.7$ ,  $\log(\text{Ca/He}) = -12.0$ . We also used *BVR* photometry from *HST* Wide Field and Planetary Camera 2 (Provencal et al. 1997) in the hybrid fit, as no *Gaia* photometry is available for this object due to its bright companion. This white dwarf was observed with the STIS CCD G230LB grating because Procyon A would saturate a G230L NUV-MAMA observation. The G230LB grating has a known red light scattering issue (Worthy et al. 2022), and is less well flux-calibrated than the G230L grating. Therefore, the red end of the G230LB spectrum is not expected to fit well to the models. Provencal et al. (2002) found that Procyon B has a hydrogen abundance of  $\log(\text{H/He}) < -4$ , which is consistent with our abundance of  $\log(\text{H/He}) = -4.6$ .

**WD 2140+207:** The UVES spectrum of WD 2140+207 has echelle order ‘ripples’ which could be due to issues with the reduction or blaze function. We mitigated for this by binning the spectrum and smoothing it with a Savitzky–Golay filter. As shown in Fig. 11, there are gaps in the UVES spectrum at the location of two of the Swan bands, centred at 4737 Å and 5636 Å, and therefore only one Swan band could be fitted, which led to degeneracies in the solution. We found that adding hydrogen at an abundance of  $\log(\text{H/He}) = -5.2$  to the C + He models resulted in a better fit to the spectrum and SED of WD 2140+207, and therefore the final best-fitting solution for this white dwarf contains a trace hydrogen abundance.

Three of the seven DQ white dwarfs in the 13 pc sample required some level of hydrogen to fit the UV and optical data. This result is in contrast to the discussion of Coutu et al. (2019), who only found evidence of hydrogen in two out of a sample of 293 optical observations of DQs below 10 000 K. They noted that the CH molecular band near 4300 Å would be visible for DQs below 8000 K given the results of their tests with  $-4.0 < \log(\text{H/He}) < -2.0$ . In our analysis including UV spectra, WD 0736+053 and WD 2140+207 have  $\log(\text{H/He})$  values of  $-4.6$  and  $-5.2$  respectively, which is at a low enough level that the CH feature is not present. WD 0548–001 has a clear CH feature and therefore a much higher  $\log(\text{H/He})$  of  $-3.7$ .

To test the impact of hydrogen, we fitted the remaining DQ white dwarfs with C + H + He models with  $T_{\text{eff}}$ ,  $\log g$ , and  $\log(\text{C/He})$  fixed at their best-fitting values from the fits with C + He models,

and the hydrogen abundance was allowed to vary, to find limits on the hydrogen content. For WD 0208–510, WD 0435–088, and WD 1142–645,  $\log(\text{H/He}) = -5.5$  was determined as the upper limit of hydrogen.

Figure 12 shows the carbon abundances in DQ white dwarfs as a function of  $T_{\text{eff}}$ . We show the parameters for WD 0038–226 with green crosses, both from this work (using the Koester (2010) code) alongside those from Blouin & Dufour (2019), joined together with a line. This difference indicates the disparity between the two models at low  $T_{\text{eff}}$  and low carbon abundance. The difference between the two models for various carbon abundances is also shown on the plot, and at lower  $T_{\text{eff}}$  there are significant deviations.

Excluding the DQpec, four out of the six DQ white dwarfs in this sample have very low masses when fitted with UV data, shown in Table 8: WD 0208–510 ( $0.357 M_{\odot}$ ), WD 0435–088 ( $0.480 M_{\odot}$ ), WD 1142–645 ( $0.470 M_{\odot}$ ), and WD 2140+207 ( $0.431 M_{\odot}$ ). DQ white dwarfs are expected to have very slightly lower than average masses due to the mass-dependence of carbon dredge up (Bédard 2024). However, optical-only fits from e.g. Coutu et al. (2019) do not produce such low masses as those determined in this work. Farihi et al. (2013) determined a mass of  $0.59 M_{\odot}$  for WD 0208–510, where near-UV fluxes were not incorporated into the fit due to these same discrepancies. Coutu et al. (2019) determined a mass of  $0.55 M_{\odot}$  for WD 0435–088,  $0.58 M_{\odot}$  for WD 1142–645, and  $0.50 M_{\odot}$  for WD 2140+207. McGill et al. (2023) used the gravitational microlensing technique with *HST* WFC3 observations to determine a mass of  $0.56 \pm 0.08 M_{\odot}$  for WD 1142–645. This method is entirely independent of model atmospheres and spectroscopy. The mass of WD 1142–645 that we determined from fitting STIS UV data is  $2\sigma$  away from the microlensing mass from McGill et al. (2023) and the optical mass from Coutu et al. (2019).

Our results indicate that including STIS UV data in DQ fitting might bias the solutions towards low  $T_{\text{eff}}$  and masses. This suggests that there are issues with DQ models in the UV, which can be somewhat mitigated for by adding a substantial amount of hydrogen to the models, hence the discrepancy between our results and Coutu et al. (2019). As discussed in Section 3.2.2, we artificially decreased the  $g_f$  values in our models in order to match the UV C I line strengths. However, this does not change the full slope of the STIS spectrum, and therefore the resulting best-fit parameters are still affected.

#### 4.2.3 DBQA results

The DBQA white dwarf WD 1917–077 displays hydrogen and helium features in its optical spectrum and carbon features in its UV spectrum. We generated a grid to fit this white dwarf with  $T_{\text{eff}}$ ,  $\log(\text{C/He})$  and  $\log(\text{H/He})$  allowed to vary, and  $\log g$  fixed. The DBQA grid spans  $T_{\text{eff}} = 10\,000 - 11\,000$  K in steps of 250 K,  $\log(\text{C/He}) = -5.0$  to  $-6.0$  in steps of 0.25 dex, and  $\log(\text{H/He}) = -5.0$  to  $-6.0$  in steps of 0.5 dex. The  $\log g$  in the models was fixed at 8.05, which was determined by a fit to *Gaia* photometry (O’Brien et al.

**Table 8.** Best-fit parameters for helium-atmosphere white dwarfs with carbon bands within 13 pc of the Sun. Symbols indicate the photometry used for the fit. No symbol indicates *Gaia*, 2MASS and WISE. ‡ indicates *BVRI* photometry was used in the fit. § indicates no photometry was used in the fit.

WD name	SpT	$T_{\text{eff}}$ (K)	$\log g$	Mass ( $M_{\odot}$ )	$\log(\text{C}/\text{He})$	$\log(\text{H}/\text{He})$	$\log(\text{Mg}/\text{He})$	$\log(\text{Ca}/\text{He})$	$\log(\text{Fe}/\text{He})$
0038–226	DQpec	$5604 \pm 8$	$8.152 \pm 0.008$	$0.666 \pm 0.005$	$-8.93 \pm 0.03$	–	–	–	–
0208–510 §	DQ	$7427 \pm 27$	$7.574 \pm 0.02$	$0.357 \pm 0.008$	$-5.81 \pm 0.03$	$< -5.5$	–	–	–
0435–088	DQZ	$6310 \pm 5$	$7.837 \pm 0.005$	$0.480 \pm 0.003$	$-6.67 \pm 0.01$	$< -5.5$	$-12.7 \pm 0.2$	–	–
0548–001	DQH	$6117 \pm 8$	$8.216 \pm 0.007$	$0.709 \pm 0.005$	$-6.15 \pm 0.02$	$-3.7 \pm 0.1$	–	–	–
0736+053 ‡	DQZ	$7633 \pm 3$	8.03 (fixed)	$0.594 \pm 0.001$	$-5.68 \pm 0.03$	$-4.6 \pm 0.1$	$-10.4$ (fixed)	$-12.0$ (fixed)	$-10.7$ (fixed)
1142–645	DQ	$7510 \pm 6$	$7.812 \pm 0.005$	$0.470 \pm 0.003$	$-5.90 \pm 0.01$	$< -5.5$	–	–	–
1917–077	DBQA	$10785 \pm 2$	8.05 (fixed)	$0.612 \pm 0.001$	$-5.27 \pm 0.02$	$-5.55 \pm 0.1$	–	–	–
2140+207	DQ	$7765 \pm 10$	$7.735 \pm 0.007$	$0.431 \pm 0.003$	$-6.29 \pm 0.02$	$-5.2 \pm 0.1$	–	–	–

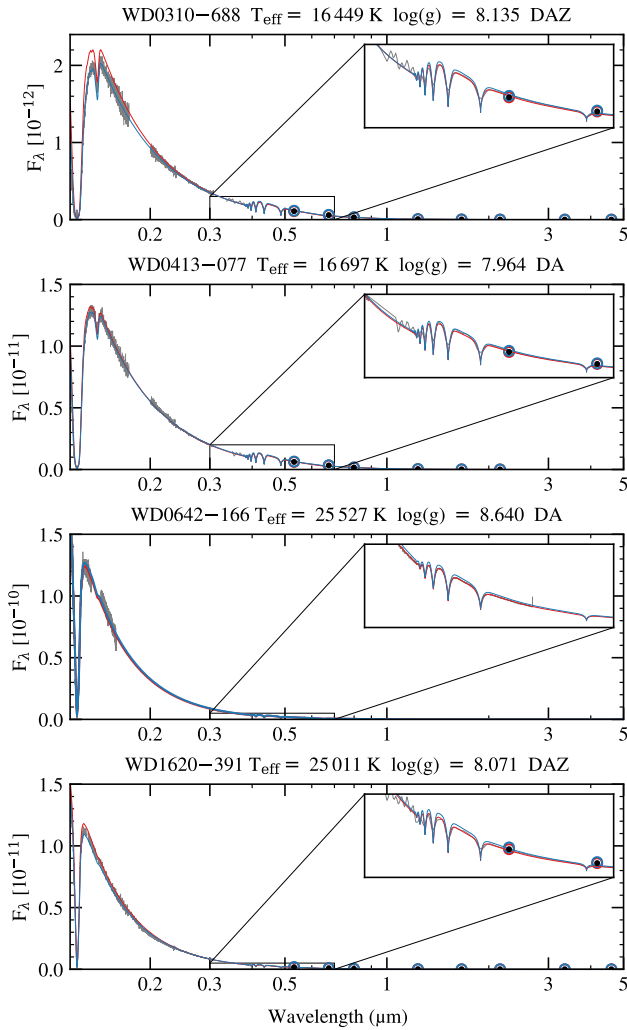


**Figure 3.** Hybrid spectrophotometric fits of H-atmosphere white dwarfs in the 13 pc sample with high-resolution STIS spectra. Flux is given in units of  $\text{erg cm}^{-2} \text{s}^{-1} \text{\AA}^{-1}$ . The blue models are best fits to STIS spectra plus *Gaia*, 2MASS, and WISE photometry, where available. The red models are the fits to just the *Gaia*, 2MASS, and WISE photometry. All parameters in this figure are from the fits to just optical/IR data (red models), as these do not suffer from issues of flux calibration. For WD 0642–166, the red model is the fit to just the flux-calibrated G430L spectrum, and the blue model is the fit to the G430L spectrum plus the E140H spectrum that has been scaled.

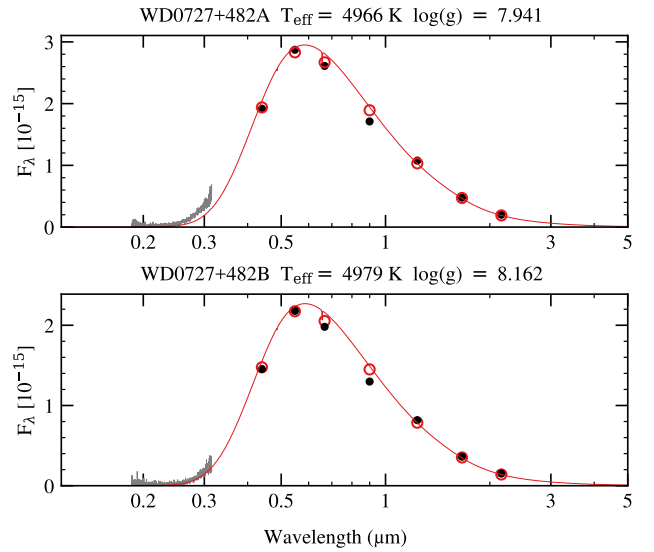


**Figure 4.** Photometric fits for the wide DA + DA system WD0727+482 A+B. Reliable *Gaia* photometry is not available for these stars so archival *BVRI* optical photometry is used in the fit instead. The STIS spectra were not included in the fit but are plotted for completeness.

2024). An iterative fitting method was used: the optical and infrared photometry was fitted for  $T_{\text{eff}}$ , and the STIS and COS spectra plus the X-shooter spectrum were fitted for  $\log(\text{C}/\text{He})$  and  $\log(\text{H}/\text{He})$ . We did not include the STIS and COS spectra in the photometric fit due to suboptimal flux calibration. The best-fitting parameters for WD 1917–077 are in Table 8, and the best-fitting model is shown in Fig. 13. Our best-fitting model at  $\log(\text{C}/\text{He}) = -5.27$  adequately reproduces the depth of almost all carbon lines in the UV, except for C I 1432.1 Å and C I 1751.8 Å (see middle panel of Fig. 13). The results of our fit differ from those of Oswalt et al. (1991), who fitted a UV spectrum of WD 1917–077 and determined  $\log(\text{C}/\text{He}) = -6.7 \pm 0.2$  using only one line: C I 2479 Å, observed with the International Ultraviolet Explorer spectrograph.

#### 4.2.4 DZ results

The best-fitting parameters and abundances for the DZ white dwarfs within 13 pc are presented in Table 9, and fits are shown in Fig. 14. Each DZ white dwarf required tailored modelling, and we discuss them individually below.

**WD 0046+051:** We classified WD 0046+051 (van Maanen 2) as

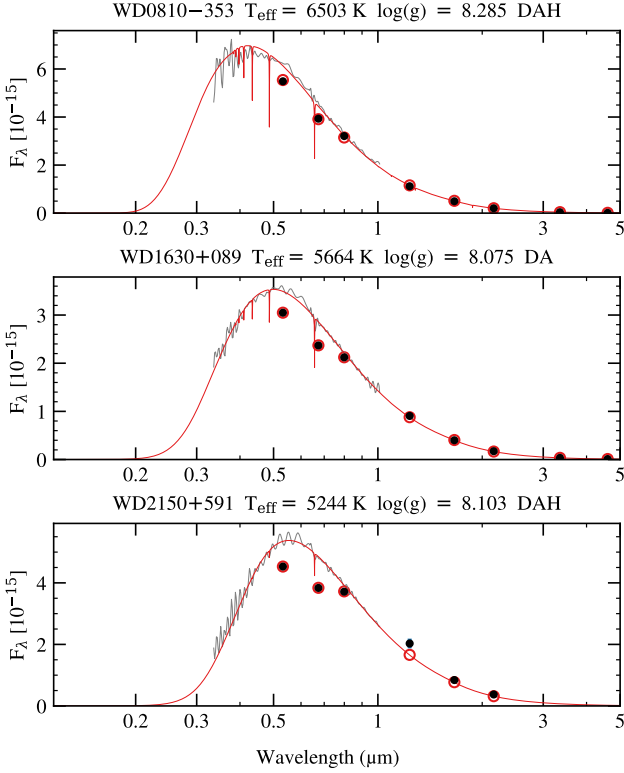


**Figure 5.** Fits to photometry of DA white dwarfs within 13 pc for which no STIS spectra are available. Flux is given in units of  $\text{erg cm}^{-2} \text{s}^{-1} \text{\AA}^{-1}$ . The red models show the fits to the photometry.

a DZA owing to a very weak and narrow  $H\alpha$  line in its X-shooter spectrum. The X-shooter spectrum also shows  $\text{Ca I}$ ,  $\text{Ca II}$ ,  $\text{Fe I}$ ,  $\text{Cr I}$ ,  $\text{Ni I}$  and  $\text{Na I}$  features. The STIS spectrum displays  $\text{Fe II}$ ,  $\text{Si I}$ ,  $\text{Mg I}$  and  $\text{Mg II}$  features. The  $T_{\text{eff}}$  and hydrogen content required for the observed weak and narrow  $H\alpha$  feature is significantly discrepant with the  $T_{\text{eff}}$  and hydrogen abundance found from fitting the full SED and metal lines. Similar issues have been identified for  $H\alpha$  in many cool, helium atmosphere metal enriched white dwarfs (see O’Brien et al. 2025 for details). Therefore, we opted not to fit  $H\alpha$  in the spectrum of WD 0046+051 and instead we constrained the hydrogen abundance from the hybrid SED fit and metal line widths.

Using Lorentzian profiles for all silicon lines in the near-UV, we were unable to achieve an adequate fit to the STIS spectrum. The 2500  $\text{\AA}$   $\text{Si I}$  multiplet showed a strong bluewards asymmetry suggesting broadening by neutral helium. In the absence of bespoke unified profiles, we used quasi-static profiles described by Walkup (1982) to model these lines, which provided an improved fit. Our results motivate calculations for silicon lines broadened by neutral helium for future analyses. We believe this fit to the spectra and photometry of van Maanen 2 to be the best published fit to date.

**WD 0552–041:** This white dwarf only shows  $\text{Ca II H}$  and  $\text{K}$  lines in the optical, and has no metal features in the UV. The STIS spectrum of this star has almost zero flux, due to its low  $T_{\text{eff}}$  and line blanketing from metals. Blouin et al. (2018) presented a detailed study of WD 0552–041 (LP 658-2), using their state-of-the-art models to fit optical and UV spectra. They were able to achieve a good fit to the  $\text{Ca II H}$  and  $\text{K}$  lines as well as the full SED by incorporating trace magnesium in the models at a level that did not produce spectral features. They also determined  $\log(\text{H}/\text{He}) < -5$ , as any more hydrogen would

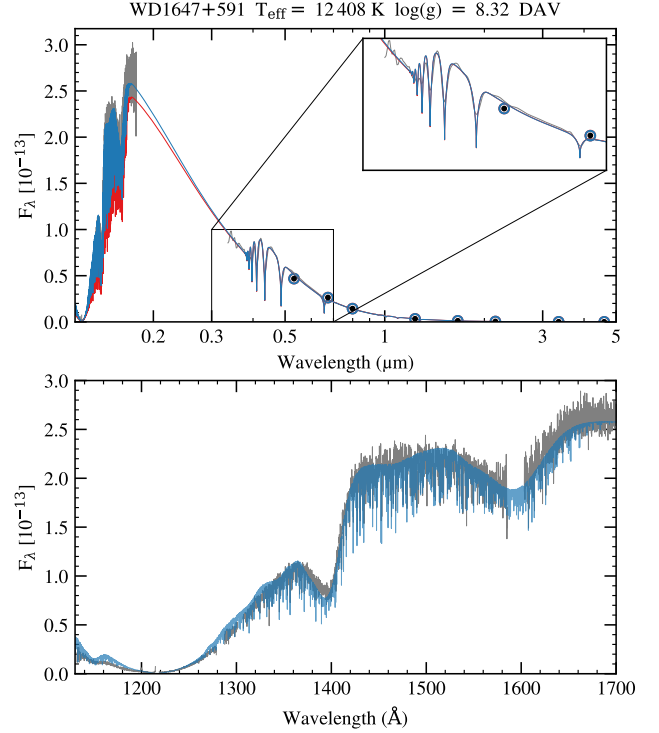


**Figure 6.** Fit of the COS G130M and G160M spectra plus photometry of WD 1647+591, using Tremblay et al. (2013) models with additional  $\text{H}_2$  molecular lines. The blue model is the best fit to the COS spectrum. The red model is the fit to just the *Gaia*, 2MASS, and WISE photometry. The parameters in this figure are from the fit to the COS spectrum (blue models). The upper panel shows the full SED fit, and the lower panel is a zoom-in of the region with  $\text{H}_2$  molecular lines. Flux is given in units of  $\text{erg cm}^{-2} \text{s}^{-1} \text{\AA}^{-1}$

cause noticeable CIA which is not present in the data. Influenced by the Blouin et al. (2018) fit, we also incorporated magnesium into our models at a level that did not produce features. We determined  $\log(\text{H}/\text{He}) = -5$ , which provided a balance that reproduced the blue slope and limited the impact of CIA in the models.

**WD 0738–172:** This is a well-known metal enriched white dwarf, which is warmer than the other DZ white dwarfs within 13 pc, enabling a straightforward model fit. No STIS spectrum is available for this white dwarf, so we instead fitted a spectrum from *HST* FOS, first published by Koester & Wolff (2000). The optical spectrum has  $\text{Ca II H}$  and  $\text{K}$  lines as well as an  $H\alpha$  line, which we fitted alongside the SED to determine the hydrogen abundance. The UV spectrum displays  $\text{Fe II}$ ,  $\text{Si I}$ ,  $\text{Mg I}$  and  $\text{Mg II}$  lines. The calcium and hydrogen abundances we determined are similar to recent measurements from Koester & Wolff (2000); Dufour et al. (2007); Coutu et al. (2019), with the magnesium abundance being slightly lower than that of Koester & Wolff (2000). The feature that is not well-modelled at  $\approx 2470 \text{\AA}$  is likely from  $\text{Fe I}$ .

**WD 1132–325:** No metals are visible in the optical spectrum of this star, and therefore this white dwarf has historically been classified as a DC. In the STIS spectrum there is a very broad  $\text{Mg I}$  line. Following the Sion et al. (1983) spectral type classification system, this would be a ‘DC with UV metals’. However, this white dwarf is effectively part of the DZ class. The  $\text{Mg II}$  doublet in the STIS spectrum is barely visible, and the spectrum is dominated by a broad  $\text{Mg I}$  ‘knee’. We measured the hydrogen abundance from the  $\text{Ly } \alpha$

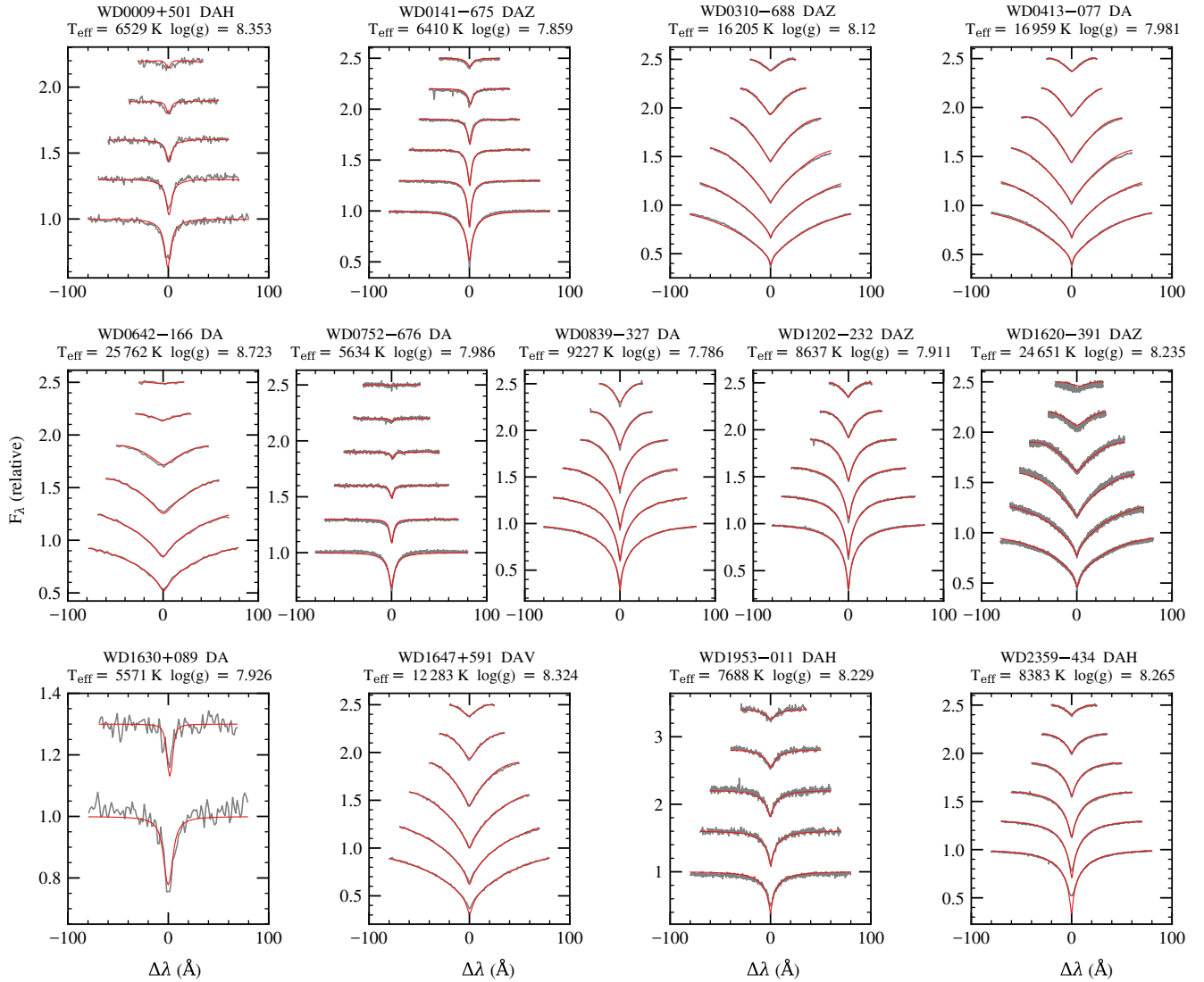


**Figure 7.** Fits of Balmer lines for white dwarfs in the 13 pc sample. Flux is given in units of  $\text{erg cm}^{-2} \text{s}^{-1} \text{\AA}^{-1}$ . Balmer lines are offset vertically for visual clarity, with H  $\alpha$  at the bottom of each plot.

red wing and Mg I line width, and also determined an upper limit on the calcium abundance using an optical spectrum (Giammichele et al. 2012).

**WD 1917+386:** Similarly to WD 1132-325, no metals are visible in the optical spectrum of this star, meaning up until now it has been classified as a DC. We re-classify it as a DZ, as it shows Mg I and Mg II lines in the UV. We incorporated the STIS spectrum into the hybrid fit by masking the magnesium lines, and we measured the hydrogen abundance from the Ly  $\alpha$  red wing. We also determined an upper limit on the calcium abundance by measuring the effect of calcium on the shape and strength of the magnesium lines.

**WD 2251-070:** This DZ is so cool and UV-faint that the STIS G230L grating was unable to detect any near-UV flux. In the optical, there are Ca I, Ca II and Na I lines. The optical spectrum also shows a broad unidentified feature near 4500 Å. A similar unexplained feature was identified by Blouin et al. (2019a) in the cool DZ WD 2356-209. Blouin et al. (2019a,b) fitted the Ca I and Ca II features of WD 2251-070 using independent models, constraining

$\log(\text{Ca}/\text{He}) = -9.8$  and  $\log(\text{H}/\text{He}) \leq -4.5$ . Our best-fitting model in Fig. 14 required a substantial amount of magnesium for a good fit to the SED, similar to WD 0552-041. For Ca I, our unified profile does not reach deep enough, but does show the expected bluewards asymmetry. For sodium, the highly broadened line wings blend into the continuum, but a line core remains that is narrower than in the data, suggesting the upper atmosphere is even denser than in our already dense model. We found a limit of  $\log(\text{H}/\text{He}) < -5.5$ , as above this abundance CIA features appear in the model that are not in the data. WD 2251-070 is 4041 K, making it one of the coolest known metal enriched white dwarfs (Elms et al. 2022; O'Brien et al. 2023; Kaiser et al. 2025). The spectroscopic fit to WD 2251-070 highlights the limitations of our models at low  $T_{\text{eff}}$  and high density.

### 4.3 Unknown composition white dwarfs

Two of the white dwarfs in the 13 pc sample, WD 1748+708 and WD 1900+705, are very strongly magnetic, with fields of 300 MG

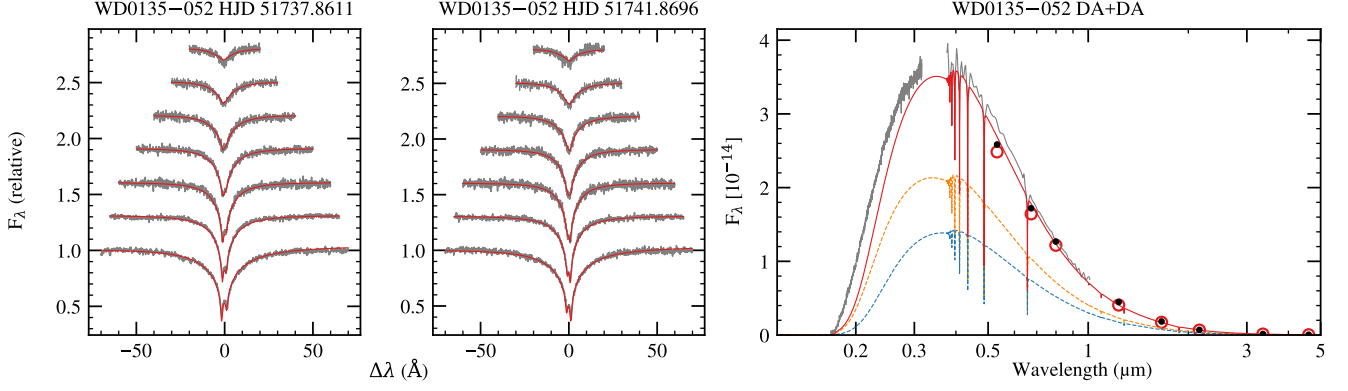


**Figure 8.** Combined fits of Balmer lines and photometry for the unresolved double-lined double white dwarf WD0135–052 in the 13 pc sample. Flux is given in units of  $\text{erg cm}^{-2} \text{s}^{-1} \text{\AA}^{-1}$ . Balmer lines are offset vertically for visual clarity, with  $\text{H } \alpha$  at the bottom of each plot. The STIS spectrum was not included in the fit but is shown on the plot. The orange and blue dashed models are the two individual models that best fit to the spectrum at HJD 51741.8696, which are then combined to form the red model.

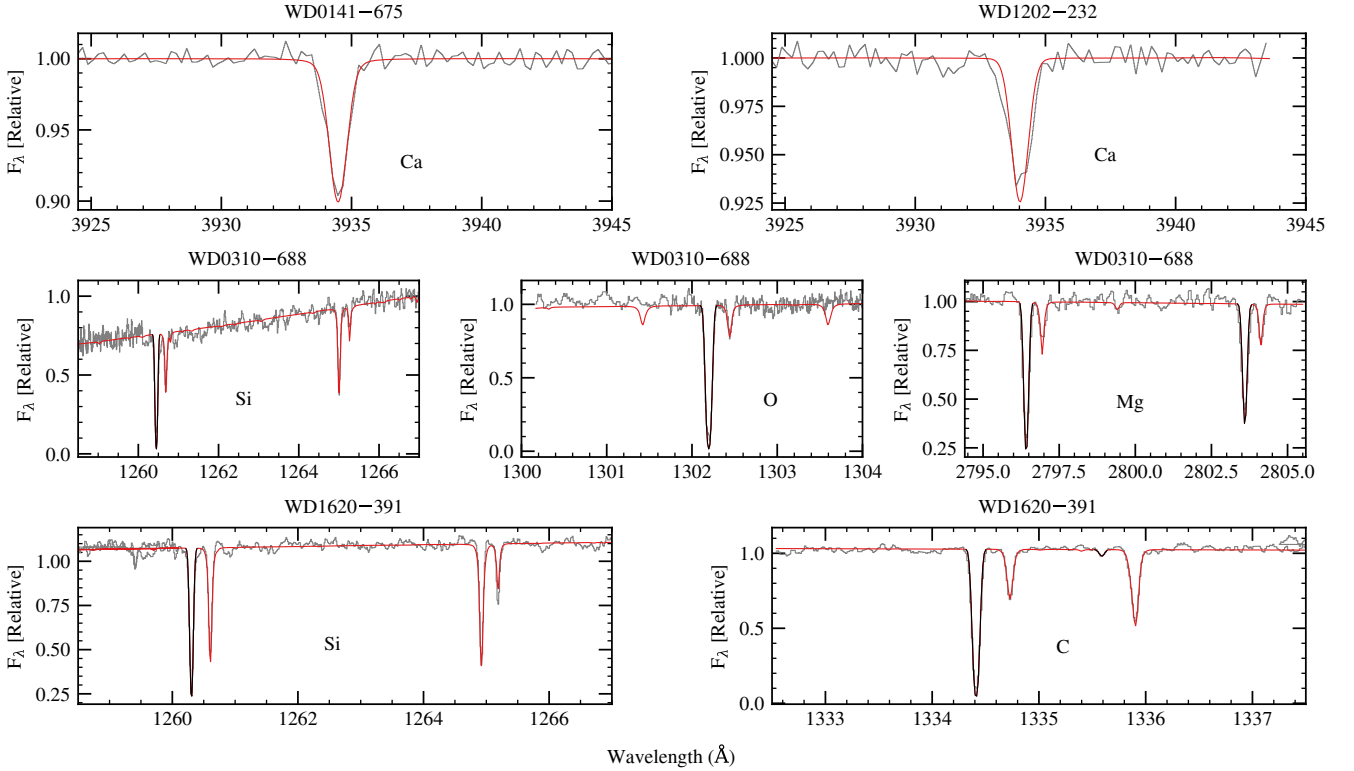


**Figure 9.** Fits to metal lines in H-atmosphere white dwarfs in the 13 pc sample. Flux is given in units of  $\text{erg cm}^{-2} \text{s}^{-1} \text{\AA}^{-1}$ . The red models are the fits to the photospheric metal features, and the black portions are Gaussian fits to the interstellar lines.

and 200 MG respectively (Bagnulo & Landstreet 2021). The strong magnetic fields cause the spectral features of both white dwarfs to become distorted and blended, therefore making it challenging not only to fit the spectra but to identify the atmospheric composition of the stars. WD 1900+705 (Grw+70°8247) was the first white dwarf in which a magnetic field was detected (Kemp et al. 1970). Ferrario et al. (2015) reported a pure-H atmosphere for this star. Hardy et al. (2023a,b) could not fit the spectrum of WD 1900+705

with state-of-the-art magnetic models, but classified it as a non-DA. WD 1748+708 (G240–72) was discovered to be magnetic by Angel et al. (1974), and the current consensus is that it has a helium-rich or carbon-rich atmosphere. Fig. 15 shows the complex splitting in both white dwarf spectra. Both WD 1748+708 and WD 1900+705 display broad-band circular polarisation of their continua (Berdyugin et al. 2022). Due to their uncertain atmospheric compositions, we classify WD 1748+708 and WD 1900+705 as DXH in Table 2. Approx-

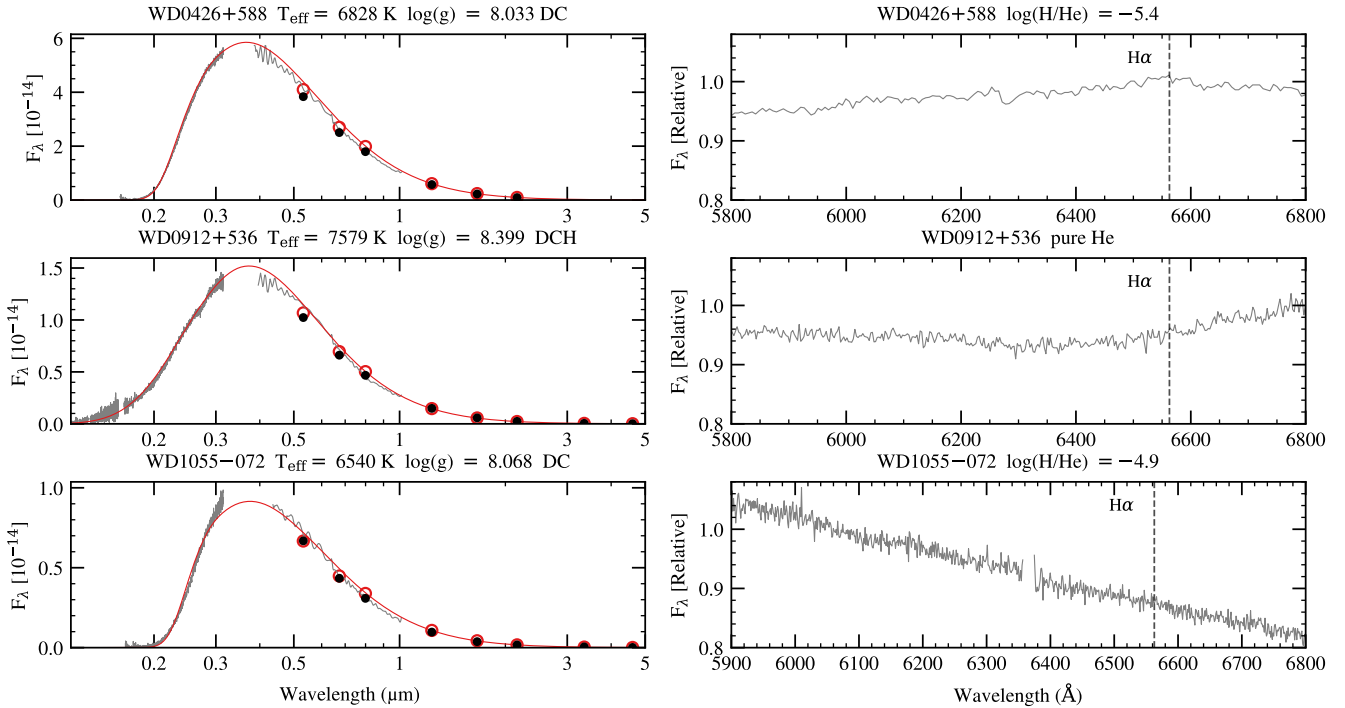


**Figure 10.** Hybrid spectrophotometric fits of white dwarfs in the 13 pc sample with He-rich atmospheres that fit best with He (+H) models. Flux is given in units of  $\text{erg cm}^{-2} \text{s}^{-1} \text{\AA}^{-1}$ . *Left*: hybrid fits to the full SED, where the red models are best fits to STIS spectra plus *Gaia*, 2MASS, and WISE photometry, where available. *Right*: optical spectra covering the  $\text{H}\alpha$  region, where the dashed lines indicate where an  $\text{H}\alpha$  feature would be present. The 100 MG field in WD0912+536 would distort and split  $\text{H}\alpha$ .

**Table 9.** Best-fit parameters for helium-atmosphere white dwarfs within 13 pc of the Sun that are enriched by metals. Symbols indicate the data used for the fit. No symbol indicates STIS, *Gaia*, 2MASS and WISE. \* indicates *Gaia* and 2MASS. ‡ indicates that no flux-calibrated STIS spectrum was available for the hybrid fit.

WD name	SpT	$T_{\text{eff}}$ (K)	$\log g$	Mass ( $M_{\odot}$ )	$\log(\text{H}/\text{He})$	$\log(\text{Ca}/\text{He})$
0046+051	DZA	$5830 \pm 15$	$8.09 \pm 0.02$	$0.627 \pm 0.013$	$-4.4 \pm 0.1$	$-10.14 \pm 0.03$
0552-041	DZ	$4642 \pm 9$	$8.098 \pm 0.007$	$0.629 \pm 0.005$	$-5.0 \pm 0.5$	$-11.07 \pm 0.06$
0738-172 ‡	DZA	$7450 \pm 87$	$7.972 \pm 0.029$	$0.559 \pm 0.017$	$-3.50 \pm 0.05$	$-10.83 \pm 0.02$
1132-325 *	DZ	$5178 \pm 1$	$8.024 \pm 0.002$	$0.583 \pm 0.001$	$-6.5 \pm 0.1$	$< -12.5$
1917+386	DZ	$5743 \pm 2$	$7.939 \pm 0.002$	$0.534 \pm 0.001$	$-5.7 \pm 0.2$	$< -13.5$
2251-070 ‡	DZ	$4041 \pm 17$	$7.99 \pm 0.02$	$0.561 \pm 0.012$	$< -5.5$	$-10.6 \pm 0.05$
WD name	$\log(\text{Mg}/\text{He})$	$\log(\text{Fe}/\text{He})$	$\log(\text{Si}/\text{He})$	$\log(\text{Na}/\text{He})$	$\log(\text{Cr}/\text{He})$	$\log(\text{Ni}/\text{He})$
0046+051	$-8.6 \pm 0.2$	$-9.3 \pm 0.1$	$-8.6 \pm 0.2$	$-9.6 \pm 0.1$	$-10.83 \pm 0.07$	$-10.97 \pm 0.05$
0552-041	$-9.5 \pm 0.5$	–	–	–	–	–
0738-172 ‡	$-9.7 \pm 0.1$	$-10.12 \pm 0.02$	$-9.40 \pm 0.1$	–	–	–
1132-325 *	$-11.38 \pm 0.05$	–	–	–	–	–
1917+386	$-10.58 \pm 0.04$	–	–	–	–	–
2251-070 ‡	$-8.5 \pm 0.2$	–	–	$-10.6 \pm 0.3$	–	–

mate parameters determined by Vincent et al. (2024) are as follows:  $T_{\text{eff}} = 5667$  K and  $\log g = 8.35$  for WD 1748+708 and  $T_{\text{eff}} = 11\,547$  K and  $\log g = 8.53$  for WD 1900+705.

## 5 DISCUSSION

### 5.1 Hybrid fitting

Saumon et al. (2014) analysed white dwarfs cooler than 6000 K with STIS observations to test the effect of the  $\text{Ly}\alpha$  red wing opacity in white dwarf models. They generated photometric datapoints by binning the STIS spectra, before fitting them in combination with optical and IR photometry. They compared optical plus IR photometric fits to STIS plus optical plus IR fits, and concluded that their parameters

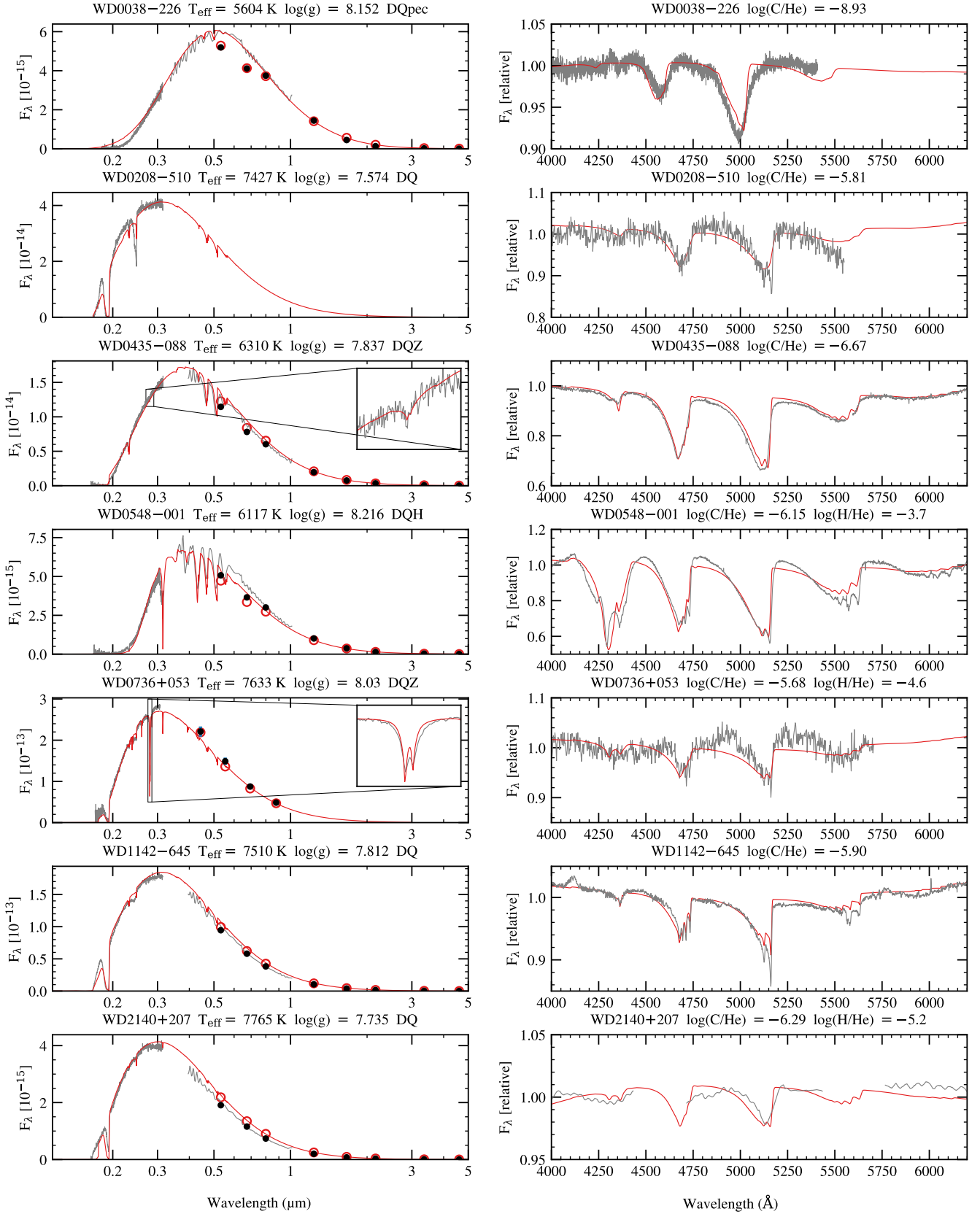


**Figure 11.** Hybrid spectrophotometric fits of DQ white dwarfs in the 13 pc sample with carbon absorption lines. *Left:* hybrid fits to the full SED. *Right:* fits to the optical Swan bands. Inset plots show the Mg II 2800  $\text{\AA}$  doublet. The carbon lines in the UV have been adjusted to match the observations.

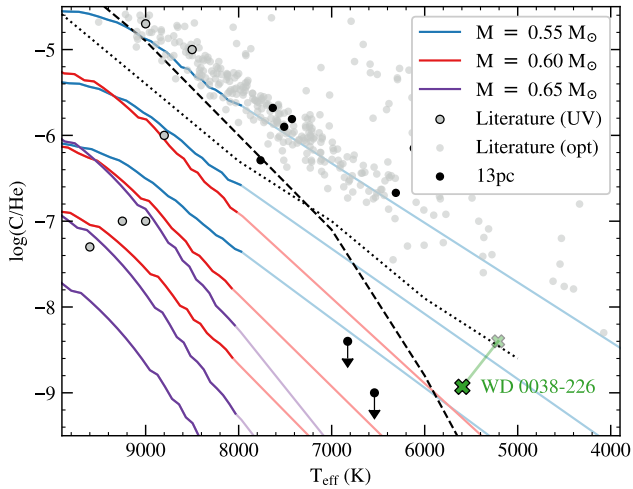


**Figure 12.** Atmospheric carbon abundance as a function of temperature for DQ white dwarfs. The background sources shown in grey are from [Blouin & Dufour \(2019\)](#); [Coutu et al. \(2019\)](#); [Tremblay et al. \(2020\)](#); [O'Brien et al. \(2023, 2024\)](#). The filled black circles represent 13 pc carbon detections and the arrows represent upper limits on carbon found in the 13 pc DC white dwarfs. The green cross is our fit to the DQpec WD 0038–226, with the faded cross being a fit to the same object by [Blouin & Dufour \(2019\)](#). The hollow black circles represent DQs with UV carbon detections from the International Ultraviolet Explorer ([Weidemann & Koester 1995](#)). The solid lines show predicted sequences of carbon dredge-up assuming different white dwarf masses and envelope carbon mass fractions (from bottom to top: 0.2, 0.4, and 0.6; [Bédard et al. 2022b](#); [Kilic et al. 2025](#)). A standard envelope thickness of  $\log q = -2$  was adopted. The sequences were linearly extrapolated below 8000 K, where they are shown in a faded colour. The black lines show the carbon detection limits: [Koester \(2010\)](#) (dashed), and [Blouin et al. \(2018\)](#) (dotted) with SNR = 5.0.

agreed within uncertainties and there was no systematic offset. They also found that incorporating STIS data into their fits halved the  $T_{\text{eff}}$  uncertainty. The parallaxes used by [Saumon et al. \(2014\)](#) were ten times less precise than the more recent *Gaia* parallaxes, and the analysis of [Saumon et al. \(2014\)](#) additionally differs from ours due to their binning of the STIS spectra. We opted to include the full information from the STIS spectra, since compared to [Saumon et al. \(2014\)](#) the 13 pc sample provides a wider  $T_{\text{eff}}$  range and greater spectral diversity, including features such as carbon and Ly  $\alpha$  lines. The two fits presented in our work – STIS + *Gaia* + IR and *Gaia* + IR only – are largely independent, as the former is primarily constrained by the UV spectra, except in the case of the coolest white dwarfs. We were therefore able to identify a discrepancy between the fits to UV data and to optical/IR data. The additional precision of *Gaia* photometry has also enabled reductions to the magnitudes of our  $T_{\text{eff}}$  and  $\log g$  fitting uncertainties compared to those presented in [Saumon et al. \(2014\)](#).

Fig. 2 demonstrates that neither our UV-dominated fits nor our optical plus IR fits are a good visual match across all wavelengths. This discrepancy is quantified in Fig. 16 for both  $T_{\text{eff}}$  and  $\log g$ . For  $T_{\text{eff}} < 10000$  K, which corresponds to the spectra with flux-calibrated STIS G230L data, the hybrid  $T_{\text{eff}}$  values are systematically 2–6 per cent larger than the photometric  $T_{\text{eff}}$  values. The hybrid  $\log g$  values are also larger than the photometric  $\log g$  values by  $\approx 0.15$  dex. These differences are smaller for the lowest  $T_{\text{eff}}$  members of the sample, because at these temperatures the STIS spectra have minimal flux and therefore do not provide much new information for the fit. All

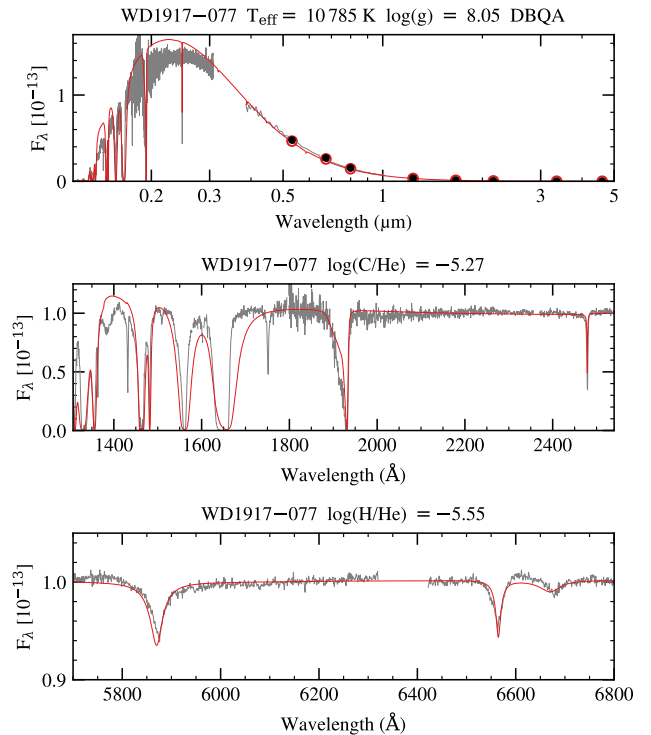


**Figure 13.** *Top:* A hybrid spectrophotometric fit to the DBQA white dwarf WD 1917–077. *Middle:* The fit to COS and STIS spectra focusing on the region with carbon features. *Bottom:* The fit to the X-shooter spectrum covering H  $\alpha$  and the He II 5876 Å line. In all plots, flux is given in units of  $\text{erg cm}^{-2} \text{s}^{-1} \text{Å}^{-1}$ . The model reproduces the depth of almost all carbon lines, except for C I 1432.1 Å and C I 1751.8 Å.

these fits rely on 3D model atmospheres (available for  $T_{\text{eff}} > 6000$  K) that do not have a free parameter for the convective mixing-length. Through testing, we found that using standard 1D models instead of the 3D models does not solve the UV-optical discrepancy. A similar offset is seen in Fig. 16 for the comparison of Balmer line fits to the hybrid fits (see also [Sahu et al. 2023](#)).

In contrast to the cooler white dwarf G230L observations, the hottest DA white dwarfs in the sample (Fig. 3) have substantially smaller hybrid  $T_{\text{eff}}$  values than photometric. [Sahu et al. \(2023\)](#) analysed COS spectra of DA white dwarfs with temperatures of  $12000 < T_{\text{eff}} < 33000$  K, and found that the COS  $T_{\text{eff}}$  values were 3 per cent lower than optical Balmer line fits. This result provides another hint that there may be a reversal in the trend of UV vs optical parameters at higher  $T_{\text{eff}}$ .

The so-called low-mass issue, which has been discussed extensively in previous studies, highlights that masses of white dwarfs cooler than 6000 K were under-predicted by up to 30 per cent when calculated using optical photometric fitting ([Hollands et al. 2018b](#); [Caron et al. 2023](#); [O'Brien et al. 2024](#); [Sahu et al. 2025b](#)). Correcting the  $\text{H}_3^+$  partition function in our models (see Section 3) reduced the effects of the low-mass issue substantially, although a significant residual discrepancy remains at the lowest temperatures depending on the exact Ly  $\alpha$  and CIA opacity sources used in the code. Modelling opacities in the UV-to-IR range for these cool white dwarfs remains a challenge ([Blouin et al. 2024](#); [Sahu et al. 2025b](#)), and hence issues with opacity modelling could still be a cause of the discrepancies between our fits with and without STIS data for  $T_{\text{eff}} < 10000$  K.

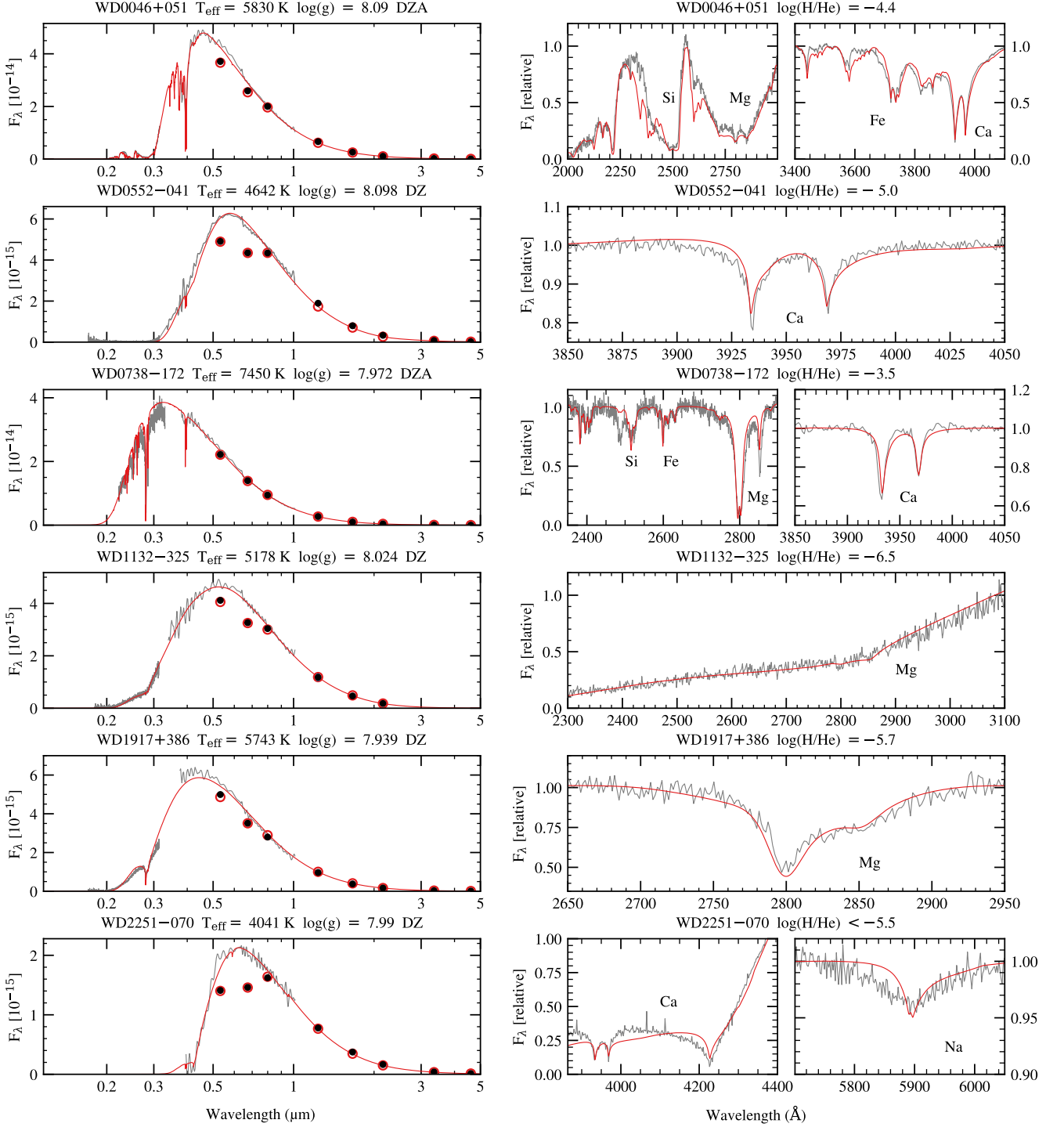


**Figure 14.** Hybrid spectrophotometric fits of DZ white dwarfs in the 13 pc sample with metal absorption lines. *Left:* hybrid fits to the full SED. *Right:* fits to the metal features.

The STIS low-dispersion gratings, including G230L which is used in our hybrid fits, were found by [Elms et al. \(2024\)](#) to be flux calibrated to within 3 per cent. [Elms et al. \(2024\)](#) also found that *Gaia* photometry is typically uncertain by  $\approx 0.01$  mag. We therefore tested the impact of STIS flux calibration and *Gaia* photometric uncertainty on the resulting  $T_{\text{eff}}$  and  $\log g$  uncertainties determined from our

hybrid fits to the 13 pc DA white dwarfs. For this test we performed a Monte Carlo analysis, in which the STIS spectra error bars were inflated between their nominal values and 3 per cent of the flux, and the *Gaia* magnitude error bars were inflated between their nominal values and 0.01 mag. These perturbations were both set to follow a normal distribution, and we did 200 iterations of the least-squares fit

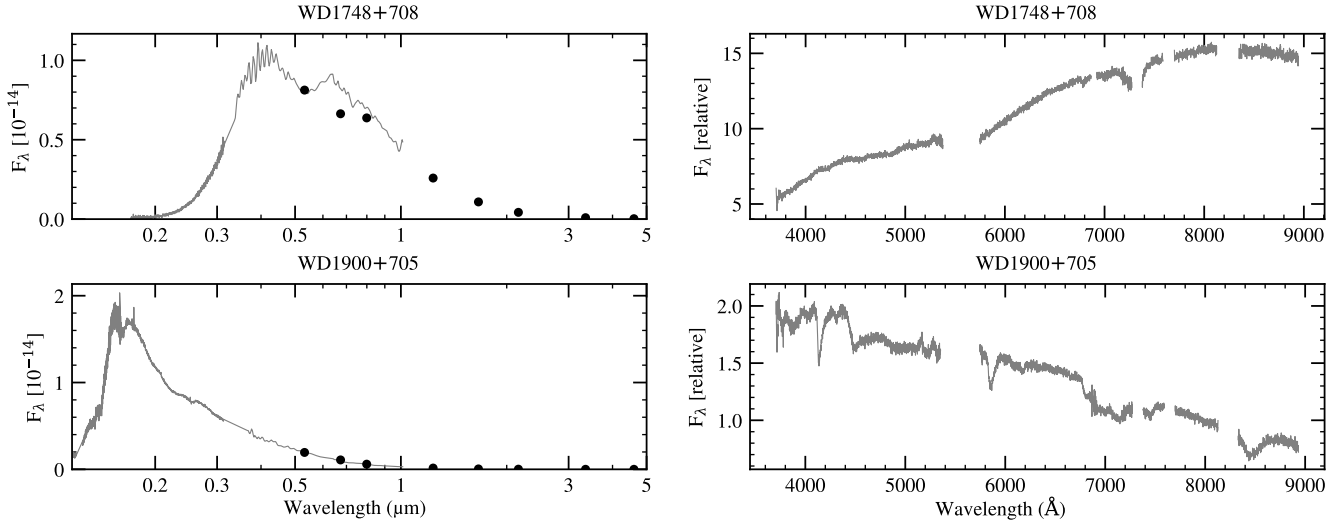


**Figure 15.** Spectra and photometry of strongly magnetic white dwarfs with unconstrained spectral types in the 13 pc sample. *Left:* STIS *Gaia* XP spectra, plus *Gaia*, 2MASS and WISE photometry. *Right:* WHT ISIS optical spectra.

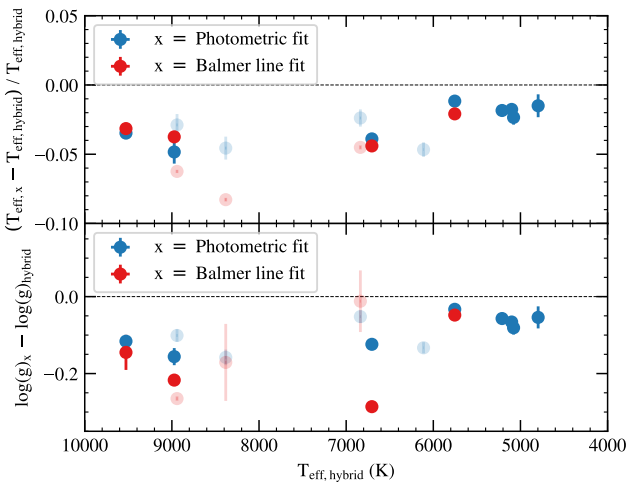


**Figure 16.** Comparisons of  $T_{\text{eff}}$  (top panel) and  $\log g$  (bottom panel) for He-atmosphere white dwarfs fitted with different methods. In blue is the difference between the photometric optical and IR fit, compared to the parameters derived from the hybrid STIS G230L, optical photometry and IR photometry fit. Also shown in red is the comparison between the Balmer line fit parameters and the hybrid parameters. Faded points correspond to magnetic white dwarfs.

with the perturbed error bars. The resulting  $1\sigma$  values were taken to be the  $T_{\text{eff}}$  and  $\log g$  uncertainties, independent of the statistical uncertainty determined initially from the least-squares fit. We found that introducing these additional observational systematic sources of uncertainty did not significantly increase the size of the error bars on the  $T_{\text{eff}}$  and  $\log g$  parameters compared to our quoted statistical error bars. We conclude that the model systematics caused by UV, optical, and IR opacities dominate in the error budget for white dwarfs in the  $T_{\text{eff}} < 10\,000$  K regime.

## 5.2 Carbon and hydrogen in He-atmosphere white dwarfs

According to spectral evolution theory, white dwarfs with helium-dominated atmospheres should have evolved from a common origin: a hot helium-rich DO white dwarf. The subsequent evolution of the spectral type, from DA/DB to DBA to DC/DQ, is mainly determined by the initial amount and distribution of hydrogen and carbon in the envelope (see [Bédard 2024](#) for a review). In particular, the convective dredge-up of carbon is expected to occur in all helium-rich objects as they cool, but only those with the thinnest primordial helium envelopes become DQ white dwarfs, while the others never display observable carbon features and thus become DC or DZ white dwarfs. This scenario predicts a continuous range of surface carbon abundances for the combined DC–DQ–DZ population at a given temperature. Convective dredge-up is also expected to be more efficient in lower-mass objects, which may explain why classical DQ white dwarfs tend to have slightly lower-than-average masses ([Bédard et al. 2022b](#)). However, hydrogen and metals can increase the opacity of the atmosphere and reduce the size of the convective zone, thus making it more challenging to detect carbon. Therefore, it could also be the case that DC and DZ white dwarfs have similar quantities of carbon to DQ white dwarfs but have more hydrogen and/or metals that suppress carbon features ([Blouin 2022](#)).

The UV coverage of our sample enabled us to place an upper limit on the abundance of carbon in the DC white dwarfs (see Section 4.2.1). Fig. 12 shows the carbon abundances of DQ white dwarfs as a function of  $T_{\text{eff}}$ . The carbon limits for the DCs are shown in context of the DQ population in Fig. 12. The carbon limits determined from the DCs were based on their UV spectra, whereas the DQ carbon abundances were determined from fitting only the optical Swan bands, so they are not directly comparable. Some DQs with purely UV carbon detections ([Weidemann & Koester 1995](#)) are indicated by hollow black circles on Fig. 12. These points lie below the main DQ cluster along with our DCs. The DC carbon limits are also model-dependent, as at these lower  $T_{\text{eff}}$  values the optical limits from two different models that were plotted in Fig. 12 vary by  $\sim 0.5$  dex. As discussed in Section 4.2.2 we also determined the abundances or upper limits on the hydrogen content of the DQ white dwarfs. The measured

hydrogen abundances are listed in Table 8, and for the remaining systems we found a consistent upper limit of  $\log(\text{H}/\text{He}) = -5.5$ . These limits are in line with the typical hydrogen abundances of DC white dwarfs (see Section 4.2.1 and Bergeron et al. 2019).

To conclude, in the small sample of stars that we tested, we found that there was no significant difference between the hydrogen content of DQ and DC white dwarfs if we take the upper limits of hydrogen in DQs to be representative of their abundances. On the other hand, we found that the DC carbon limits are well below the DQ carbon abundances at the same  $T_{\text{eff}}$  values, however the model issues identified in the UV for DQ white dwarfs, discussed in Section 4.2.2, make the direct comparison of carbon abundances derived here from UV (limits in DC) and optical spectroscopy (DQ) difficult. The DCs have an average mass of  $0.69 M_{\odot}$ , while the DQs have an average mass  $0.54 M_{\odot}$ , so this may be a first hint at an explanation for their different natures. We note that this sample size is very small, and tests on larger datasets should be carried out.

### 5.3 Radiative vs convective models

All the white dwarfs in this work were fitted with convective atmosphere models, in regimes where convection is relevant (see e.g., Figs. 7 and 11 from Saumon et al. 2022). However, for a white dwarf harbouring a magnetic field with a strength above a few tens of kG to MG depending on the atmospheric composition, convective energy transfer is expected to be suppressed in the photosphere (Tremblay et al. 2015b; Bédard et al. 2017; Gentile Fusillo et al. 2018; Cunningham et al. 2021). Therefore, a priori, radiative models should be adopted when fitting the observed spectral energy distributions of magnetic white dwarfs. We note that the effects of magnetic fields on macroscopic and atomic diffusion are different (Cunningham et al. 2021), and so this does not apply to the mixed masses, metal abundances or dredge-up of carbon.

We tested the impact of using 1D radiative models for the hybrid fits of magnetic H-atmosphere white dwarfs compared to the convective models. The convective models are described in detail in Section 3.1, and the radiative models are from Tremblay et al. (2015b) with line profiles from Tremblay & Bergeron (2009). We performed these tests on the four magnetic DA white dwarfs with STIS spectra in the 13 pc sample: WD 0009+501, WD 0553+053, WD 1953–011, and WD 2359–434. The field strengths of these stars are 250 kG, 15 MG, 500 kG, and 100 kG respectively. For the coolest pure-H atmosphere white dwarfs at 4000 K, convective energy transfer should be suppressed for field strengths above 30 kG (Cunningham et al. 2021). At higher temperatures the minimum field strength for convection suppression decreases. Given the field strengths of these four DAH white dwarfs, they are expected to experience suppression of convective energy transfer.

Bédard et al. (2017) found that WD 1953–011, WD 2359–434 and two other magnetic DAs not considered in this work fitted better in the optical with convective models. All of the 13 pc magnetic white dwarfs that were tested had larger reduced  $\chi^2$  values when fitted with the 1D radiative models, indicating a somewhat worse fit compared to the 3D convective models, for hybrid fits where both STIS was included and where STIS was not included. The parameters determined from these fits have differences of up to 500 K in  $T_{\text{eff}}$  and 0.15 dex in  $\log g$ , which is consistent with the differences between parameters determined from optical and from UV fitting with the same models, as discussed in Section 5.1. Therefore, despite the reduced  $\chi^2$  results, the convective models are not clearly preferred over the radiative models from our limited test set of magnetic white dwarfs. Gentile Fusillo et al. (2018) argued that the radiative models

provided a better fit for a case study of WD 2105–820 (a 10 000 K DAH). Here we argue that for the four stars tested in this work, convective fits are slightly better in terms of  $\chi^2$ . This subject requires a dedicated and detailed study with a larger set of magnetic DA white dwarfs.

### 5.4 Planetary material

Six white dwarfs in the 13 pc sample show metal lines in their UV spectra but not in their optical spectra: WD 0310–688 (DAZ), WD 0435–088 (DQZ), WD 0736+053 (DQZ), WD 1132–325 (DZ), WD 1620–391 (DAZ), WD 1917+386 (DZ). These systems, spanning 5500 K – 25 000 K, highlight the benefits of UV spectra to detect new metal species that are not seen in optical spectra. WD 1132–325, and WD 1917+386, which are featureless in the optical and show magnesium lines in their STIS spectra, have lower magnesium abundances than any other DZ white dwarf in the PEWDD (Williams et al. 2025). The upper limits on the calcium abundances of these two stars firmly place them as some of the least polluted white dwarfs known (Elms et al. 2022). The low abundances of these cool DZs with UV-only metals highlight the importance of observing optical DC white dwarfs in the near-UV.

#### 5.4.1 Composition of accreted material

We analysed the abundances of the 13 pc metal enriched white dwarfs using PYLLUTEDWD (Harrison et al. 2018, 2021; Buchan et al. 2022), a Bayesian inference code that determines the geological histories of planetesimals that have been accreted by white dwarfs. The results may be sensitive to the metal sinking timescale grids and the inclusion of thermohaline mixing (Buchan et al. 2025). For the H-dominated WDs, we used the timescale grids of Koester et al. (2020) as these extend to 4000 K. We excluded convective overshoot following the recommendations of Buchan et al. (2025). For the H-dominated WDs, we used grids based on the STELUM evolution code in its static mode, including 3D calibrated overshoot (Cunningham et al. 2019; Bédard et al. 2022a) for WDs at relevant temperatures (WD 0310–688 in this case), or a parametrised treatment of overshoot otherwise, as in Buchan et al. (2025). We included thermohaline mixing for systems warmer than 10 000 K. These assumptions make no qualitative impact unless otherwise noted. We added a noise floor of 0.1 dex in quadrature to the metal abundance uncertainties quoted in Tables 6 and 9.

The planetesimal masses and accretion rates inferred by PYLLUTEDWD are shown in Table 10. The accretion rates in Table 10 correspond to the mean accretion rate over the presumed accretion episode, as opposed to the diffusion flux out of the convection zone. These two quantities are often assumed to be equal for DAZ white dwarfs, but this is not the case for DZs. The metal enriched white dwarfs that only have a single metal detection or upper limit (WD 0141–675 and WD 1202–232) were not analysed further, because a single metal abundance cannot constrain any geological processes. The metal enriched white dwarfs that have two or more metal detections and/or upper limits are discussed below.

Two DAZ white dwarfs were analysed with PYLLUTEDWD. WD 0310–688 is most likely to be accreting in the steady state phase, meaning that accretion is ongoing. The low oxygen abundance in the atmosphere of WD 0310–688 implies incomplete condensation to a nominal confidence level of  $2.2 \sigma$ , but whether this process is invoked depends on the sinking timescale grid used and whether thermohaline mixing is included. Incomplete condensation occurs when volatile

**Table 10.** Masses and accretion rate outputs from the PYLLUTEDWD framework for metal enriched white dwarfs within 13 pc. Timescale grid abbreviations: *S3D* = STELUM evolution code in its static mode, including 3D calibrated overshoot (Bédard et al. 2022a), with +*T* indicating that thermohaline mixing was also included, *KN* = Koester envelope code with no overshoot (Koester et al. 2020).

WD Name	log(Mass/g)	log(Accretion rate/gs <sup>-1</sup> )	Timescale grid
0046+051	21.4 <sup>+0.2</sup> <sub>-0.2</sub>	11.2 <sup>+1.8</sup> <sub>-1.8</sub>	<i>KN</i>
0141–675	18.5 <sup>+0.4</sup> <sub>-0.4</sub>	9.0 <sup>+1.2</sup> <sub>-1.2</sub>	<i>S3D</i>
0310–688	16.8 <sup>+0.2</sup> <sub>-0.2</sub>	7.8 <sup>+0.1</sup> <sub>-0.1</sub>	<i>S3D+T</i>
0552–041	19.8 <sup>+0.5</sup> <sub>-0.5</sub>	9.2 <sup>+0.0</sup> <sub>-2.2</sub>	<i>KN</i>
0736+053	19.0 <sup>+0.4</sup> <sub>-0.3</sub>	8.2 <sup>+2.2</sup> <sub>-2.4</sub>	<i>KN</i>
0738–172	20.3 <sup>+0.3</sup> <sub>-0.3</sub>	9.8 <sup>+2.1</sup> <sub>-2.3</sub>	<i>KN</i>
1132–325	19.0 <sup>+0.5</sup> <sub>-0.3</sub>	8.0 <sup>+2.3</sup> <sub>-2.6</sub>	<i>KN</i>
1202–232	17.4 <sup>+0.5</sup> <sub>-0.6</sub>	8.2 <sup>+1.2</sup> <sub>-1.3</sub>	<i>S3D</i>
1620–391	16.9 <sup>+0.5</sup> <sub>-0.3</sub>	8.9 <sup>+0.2</sup> <sub>-0.2</sub>	<i>S3D+T</i>
1917+386	22.0 <sup>+0.3</sup> <sub>-0.3</sub>	11.6 <sup>+1.7</sup> <sub>-2.2</sub>	<i>KN</i>
2251–070	21.1 <sup>+0.4</sup> <sub>-0.5</sub>	10.4 <sup>+1.9</sup> <sub>-2.1</sub>	<i>KN</i>

elements, such as oxygen and carbon, cannot fully condense into a planetesimal, causing it to be depleted in these metals. The material accreted by WD 1620–391 could not be modelled accurately by PYLLUTEDWD, because the carbon is heavily depleted relative to silicon, after normalising to the Solar composition. This depletion does, however, imply incomplete condensation.

Six DZ(A) white dwarfs in 13 pc were also analysed with PYLLUTEDWD. In each case, PYLLUTEDWD was able to fit the abundances well, and found that the system has likely reached the declining phase of accretion (with at least 93 per cent confidence). The low Ca/Mg ratio for WD 1917+386 implies that it is particularly deep into the declining phase:  $39 \pm 3$  Myr since the end of accretion, or  $7.0 \pm 0.5 \tau_{\text{Mg}}$ , where  $\tau_{\text{Mg}}$  is the Mg sinking timescale. For WD 0046+051 (van Maanen 2), PYLLUTEDWD found evidence (to  $\sim 1.9 \sigma$  confidence) for incomplete condensation, with a characteristic temperature that implies a formation distance of around 1 au. Given that accretion is inferred to have ceased, the total mass accreted by each white dwarf can be constrained. These masses range from  $10^{19}$  to  $10^{22}$  g, corresponding to asteroids or small moons. The accretion rates are relatively poorly constrained as they are sensitive to the assumed duration of accretion events.

We additionally analysed the DQZ white dwarf WD 0736+053 (Procyon B) with PYLLUTEDWD. The abundances are close to chondritic, however the code finds evidence for incomplete condensation at  $1.5 \sigma$  confidence. The most likely phase of accretion is the declining phase, with a probability at least 85 per cent.

#### 5.4.2 Metal enrichment demographics

Statistics of white dwarf samples accreting planetary debris depends on the sample selection effects (e.g. average  $T_{\text{eff}}$  and mass, hence characteristic age), atmospheric composition, spectroscopic resolution, and wavelength coverage. A sample of high-resolution optical spectra centred around the Ca II H and K lines revealed a fraction of 25 per cent (Zuckerman et al. 2003) with metal lines. Koester et al. (2014) found that 27–50 per cent of white dwarfs were metal enriched, based on a warm ( $17\,000 \text{ K} < T_{\text{eff}} < 27\,000 \text{ K}$ ) white dwarf sample and far-UV spectroscopy. An updated far-UV study revealed that at least 40 per cent of warm ( $13\,000 \text{ K} < T_{\text{eff}} < 30\,000 \text{ K}$ ) white dwarfs are metal enriched (Ould Rouis et al. 2024). It has

also been observed that the enrichment fraction decreases significantly for larger white dwarf masses (McCleery et al. 2020; Ould Rouis et al. 2024; Cunningham et al. 2024). For the 13 pc sample, we found an enrichment fraction of  $k/N = 13/44 = 30 \pm 8$  per cent (where the error bars are  $\sqrt{N}$ ). The 13 pc sample has a median  $T_{\text{eff}}$  of 6700 K, much lower than that of the samples analysed by Zuckerman et al. (2003); Koester et al. (2014); Ould Rouis et al. (2024). Our marginally reduced fraction compared to Ould Rouis et al. (2024) may be caused by the effects of metal line visibility in our sample, given the higher average mass of a volume-limited sample compared to a magnitude-limited sample (Tremblay et al. 2016), but could also hint at a decrease of enrichment rates as a function of cooling age, as the 13 pc sample contains on average older white dwarfs (Hollands et al. 2018a).

It was shown by Koester et al. (2014) that the limiting sensitivity to accretion rates is broadly comparable between silicon detections in the ultraviolet (COS) and calcium detections in the optical (see their Figure 8). If planetary system properties (e.g. the occurrence of planetary material, disc lifetimes, and the duty cycle of disruption/accretion events) are independent of age, then the enrichment incidence measured in the UV ( $45 \pm 6$  per cent from Ould Rouis et al. 2024) should constitute a lower limit on the corresponding enrichment fraction in the 13 pc sample. This is because metal diffusion timescales are orders of magnitude longer in the (cooler) 13 pc sample, approaching  $\sim 10^6$  years, compared to timescales of order days in the COS sample (Koester et al. 2020). One thus expects to recover a similar fraction of systems in an active accretion phase, plus an additional population of white dwarfs observed during the declining phase.

The enrichment fractions measured for the two samples are consistent at the  $1.5 \sigma$  level. This is compatible with age-independent enrichment properties, but also with scenarios in which the frequency of accretion events (or the time-averaged accretion rate) decreases with time. In that case, a reduction in accreted mass would tend to lower the polluted fraction, while the increase of diffusion timescales with age would act in the opposite sense by extending the detectable “memory” of past accretion. The net effect is therefore degenerate: although it could, in principle, be explored with forward modelling, the size of the declining-phase population would depend sensitively on poorly constrained parameters (e.g. disk lifetimes and the interval between accretion episodes), making it difficult to disentangle with current data.

#### 5.5 Stellar multiplicity

Table 11 shows all confirmed 13 pc multiple-star systems containing white dwarfs. The UV has historically been significant for detecting white dwarf companions to main sequence stars, since white dwarfs are typically brighter at UV wavelengths, relative to optical wavelengths, than main sequence stars. These multiple-star systems have been identified using proper motion techniques and radial velocity measurements. We find 14 multiple-star systems out of a total of 44 systems, where each WD + WD pair is counted as a single system. Therefore the white dwarf multiplicity fraction in 13 pc is  $k/N = 14/44 = 32 \pm 9$  per cent. The frequency and diversity of these systems indicate that they must be common in the Solar neighbourhood, given that almost one in three white dwarfs are part of multiple star systems. Additionally, some of the white dwarfs within 13 pc are highly massive and/or strongly magnetic, with fields over 100 MG, and such systems could be the products of stellar mergers (Temink et al. 2020; Bagnulo & Landstreet 2022).

Using analysis from the 40 pc white dwarf sample (O’Brien et al.

2024), we determine a multiplicity fraction in the 13–40 pc shell of 19.5 percent. We used this shell to determine an independent multiplicity fraction that does not contain the 13 pc white dwarfs. Twenty percent of the 13 pc white dwarf sample is 9, compared to the 14 multiple-star systems with a white dwarf within 13 pc. Double white dwarf systems are detectable to larger distances in the optical due to their double-lined spectra or systematically low  $\log g$  values when fitted with single-star models. However, close white dwarf + main sequence binaries are more challenging to detect in the optical due to the main sequence component outshining a cool white dwarf companion. The proximity of the white dwarfs in the 13 pc sample makes the binary systems more easily resolvable, and the space-based near-UV spectra available for the sample also provide a dataset uncontaminated by companions.

Without a comprehensive radial velocity survey of the whole sky, many of our systems, if placed at a distance of 40 pc, would be missed with only optical observations. The white dwarfs in the Sirius, Procyon, 40 Eri, GJ 86, and G 203-47 systems were more easily identified due to the proximity of these systems to the Sun, enabling the white dwarf components to be resolved by *HST*. If these systems were further than a few pc away, the white dwarfs would be challenging to identify, let alone observe and characterise, due to the brightness of their main sequence companions. Additionally, if they were placed at  $\approx 100$  pc, Sirius, Procyon, 40 Eri, and GJ 86 would not be resolved by *Gaia*, which has an on-sky resolution of 0.4 arcsec.

## 5.6 Variability

White dwarfs show photometric variability for a variety of reasons, including magnetism, pulsations, and binarity. We checked all 13 pc white dwarfs to see if they showed variability in *Transiting Exoplanet Survey Satellite* (*TESS*; Ricker et al. 2015) lightcurves. All signals and non-variability limits for the 13 pc white dwarfs are listed in Table 12. Most of the sample do not show variability, to very good limits. Four of the magnetic white dwarfs show significant *TESS* periods, most likely due to spots at the rotation period. They are: WD 2359-434 at 2.695 hours, WD 0009+501 at 8.02 hours, WD 0912+536 at 31.95 hours, and WD 1953-011 at 34.62 hours. The rotation periods of the first three of these magnetic systems were identified by Oliveira da Rosa et al. (2024), who did a crowding analysis to check that the signal originated from the white dwarf, using *TESS-LOCALIZE*<sup>11</sup> (Higgins & Bell 2023). The results from *TESS-LOCALIZE* are ambiguous for WD 1953-011, but it was flagged as photometrically variable in *Gaia* which shows the *TESS* period, therefore confirming that the signal is coming from the white dwarf (Steen et al. 2024). Additionally, the well-known pulsator WD 1647+591 shows variability in its *TESS* lightcurves, and Bognár & Sódor (2024) determined a rotation period of 9.1 hours from frequency splittings in the *TESS* data. A few other white dwarfs appeared to show significant *TESS* variability signals, WD 1620-391 at 3.44 hours and WD 0839-327 at 11.43 hours, but after careful exploration with *TESS-LOCALIZE*, the signals do not appear to be coming from the white dwarf but rather another nearby star within the *TESS* field of view.

## 6 CONCLUSIONS

In this work, we analysed near-UV, optical, and IR observations of white dwarfs within 13 pc of the Sun. The main observations underpinning this work were from the STIS instrument onboard *HST*. The volume-limited 13 pc sample consists primarily of cool white dwarfs, and the STIS observations provided flux-calibrated UV data for which to test and calibrate atmosphere models. The STIS spectra enabled us to identify many new or unexpected features in the atmospheres of the white dwarfs in the sample, including the broad Mg II 2800 Å lines identified in He-rich white dwarfs with low-resolution spectra, and narrow metal lines identified in H-rich warm white dwarfs. Specifically, we identified a Mg II feature in the STIS spectra of WD 1917+386 (previously DC) and WD 0435-088 (previously DQ), and a Mg I feature in the STIS spectrum of WD 1132-325 (previously DC). The following white dwarfs in the sample only display metal features in the UV: WD 0310-688 (DAZ), WD 0435-088 (DQZ), WD 0736+053 (DQZ), WD 1132-325 (DZ), WD 1620-391 (DAZ), WD 1917+386 (DZ). Therefore optical spectroscopy alone would have missed six metal enriched white dwarfs in the sample. Additionally, carbon features are only seen in the UV for the DBQA white dwarf WD 1917-077, and H<sub>2</sub> molecular lines are detectable only in the UV for the pulsating DAV WD 1647+591.

Following our fits to the 13 pc spectra and photometry, we compared UV and optical parameters for H-atmosphere white dwarfs. We found that for  $T_{\text{eff}} < 10\,000$  K the  $T_{\text{eff}}$  from UV fitting was between 2 and 6 percent larger than the  $T_{\text{eff}}$  from optical fitting, showing that current models fail to replicate the full SED of these white dwarfs. The flux-calibrated STIS spectra of the He-rich DC white dwarfs enabled us to constrain their hydrogen content, which is not straightforward with optical photometry alone. We identified a significant discrepancy between models and observations of carbon lines in the near-UV, despite accurate modelling of the optical Swan bands. After altering the  $gf$  values for the UV C I lines to match the observations, we found systematically low masses from fitting UV observations of DQs, that are not consistent with the more typical masses of the same DQs determined from optical fitting. We analysed the difference between the hydrogen content and carbon content of DC and DQ white dwarfs. There was no measurable difference between the hydrogen content of DQs and DCs, but the upper limits of carbon in DCs were well below that of DQs. These results are model-dependent, and given the issues with modelling carbon lines in the UV, are treated with caution. The atomic data of the UV carbon lines should be revisited in order to improve future modelling efforts. We also tested the effect of fitting magnetic white dwarf spectra with radiative models as opposed to convective models, which should be a more accurate treatment of a magnetic white dwarf atmosphere. We found that neither the radiative nor convective models provided a significantly better fit. Finally, we found a 32 percent multiplicity fraction for the 13 pc white dwarfs, and at least 27 percent of the white dwarfs showed evidence of accretion of planetary debris.

The sample reveals potential avenues to improve white dwarf modelling across the UV-to-IR SED. The strength of carbon bands in the UV in current models is substantially different from observations. Metal lines in cool He-rich atmosphere white dwarfs are challenging to model, both in the UV and in the optical, and improvements must be made to the line profiles and other physics such as pressure ionisation. Observations of more optically classified DC white dwarfs would be beneficial, to reveal Mg I or Mg II features, or possible carbon lines. Flux-calibrated *JWST* NIRSpec and MIRI spectra for 35 white dwarfs within 13 pc will be collected as part of Cycle 5 (program 10131), which will provide insight into the nature of CIA

<sup>11</sup> <https://github.com/Higgins00/TESS-Localize>

**Table 11.** Details of all confirmed white dwarfs within 13 pc of the Sun that are part of a multiple-star system. Projected separations were calculated in most cases using *Gaia* DR3 data, aside from those binaries that are unresolved in *Gaia*. A colon symbol indicates that the spectral type of the star has not been confirmed. For higher-order systems (triple or quadruple) the periods separated by semicolons are the innermost to outermost periods for the hierarchical system.

Star 1 Name	Star 1 SpT	Star 2 Name	Star 2 SpT	Star 3 Name	Star 3 SpT	Star 4 Name	Star 4 SpT	Projected Separation [au]
Sirius A	A0	WD 0642–166	DA	–	–	–	–	20
Procyon A	F5	WD 0736+053	DQZ	–	–	–	–	15
40 Eri A	K1	WD 0413–077	DA	40 Eri C	M4.5	–	–	42; 417
Stein 2051 A	M4	WD 0426+588	DC	–	–	–	–	57
G 203-47 A	M3.5	G 203-47 B	DC	–	–	–	–	0.05
IRAS 21500+5903	M3	WD 2150+591	DAH	–	–	–	–	124
LP 783-2	M6.5	WD 0738–172	DZA	–	–	–	–	186
GJ 432 A	K0	WD 1132–325	DZ	–	–	–	–	146
L 923-22	M5	WD 1917–077	DBQA	–	–	–	–	285
GJ 86 A	K1.5	WD 0208–510	DQ	–	–	–	–	28
WD 0727+482 A	DA	WD 0727+482 B	DA	G 107-69 A	M4.5	G 107-69 B	dM/BD:	0.5; 8; 1161
GJ 1179 A	M5	WD 1345+238	DC	–	–	–	–	2231
WD 0135–052 A	DA	WD 0135–052 B	DA	–	–	–	–	0.03
HD 147513	G5	WD 1620–391	DA	–	–	–	–	4454

in cool white dwarfs, as well as test the optical-UV  $T_{\text{eff}}$  discrepancy that has been identified from spectral modelling.

## ACKNOWLEDGEMENTS

MOB, PET, BTG, SS and AMB received funding from the European Research Council under the European Union’s Horizon 2020 research and innovation programme numbers 101002408 (MOB, PET and AMB), and 101020057 (BTG and SS). MAH and AB acknowledge Warwick Astrophysics prize post-doctoral fellowships made possible thanks to a generous philanthropic donation.

Support for the NASA/ESA Hubble Space Telescope Program number 14076 was provided by NASA through a grant from the Space Telescope Science Institute, which is operated by the Association of Universities for Research in Astronomy, Incorporated, under NASA contract NAS5-26555. This work has made use of data from the European Space Agency (ESA) mission *Gaia* (<https://www.cosmos.esa.int/gaia>), processed by the *Gaia* Data Processing and Analysis Consortium (DPAC, <https://www.cosmos.esa.int/web/gaia/dpac/consortium>). Funding for the DPAC has been provided by national institutions, in particular the institutions participating in the *Gaia* Multilateral Agreement.

This research has made use of the SVO Filter Profile Service "Carlos Rodrigo", funded by MCIN/AEI/10.13039/501100011033/ through grant PID2020-112949GB-I00. This research has made use of NASA’s Astrophysics Data System; the SIMBAD database, operated at CDS, Strasbourg, France; and the VizieR service. This work made use of `ASTROPY`:<sup>12</sup> a community-developed core `PYTHON` package and an ecosystem of tools and resources for astronomy (Astropy Collaboration et al. 2013, 2018, 2022). This work also made use of the `PYTHON` package `SCIPY` (Virtanen et al. 2020). Computing facilities were provided by the Scientific Computing Research Technology Platform of the University of Warwick. We thank S. Blouin for sharing his finding of the reason for the overestimation of the  $H_3^+$  partition function.

<sup>12</sup> <http://www.astropy.org>

## DATA AVAILABILITY

*HST* data are available in the MAST archive, with the majority of observations falling under Program ID 14076. ESO data are available in the ESO science archive, with the majority of observations falling under Program IDs 098.D–0392(A) and 099.D–0661(A). All observation details are in Table 1. Some optical spectra used in this work were downloaded from the Montréal White Dwarf Database (Dufour et al. 2017). Reduced WHT ISIS data are available on request.

## REFERENCES

- Abel M., Frommhold L., Li X., Hunt K. L. C., 2012, *J. Chem. Phys.*, **136**, 044319
- Ali A. W., Griem H. R., 1965, *Physical Review*, **140**, 1044
- Allard N., Kielkopf J. F., 1982, *Reviews of Modern Physics*, **54**, 1103
- Allard N. F., Kielkopf J. F., 2009, *A&A*, **493**, 1155
- Allard N. F., Royer A., Kielkopf J. F., Feautrier N., 1999, *Phys. Rev. A*, **60**, 1021
- Angel J. R. P., Illing R. M. E., Landstreet J. D., 1972, *ApJ*, **175**, L85
- Angel J. R. P., Hintzen P., Strittmatter P. A., Martin P. G., 1974, *ApJ*, **190**, L71
- Astropy Collaboration et al., 2013, *A&A*, **558**, A33
- Astropy Collaboration et al., 2018, *AJ*, **156**, 123
- Astropy Collaboration et al., 2022, *ApJ*, **935**, 167
- Baer M., Proffitt C. R., Lockwood S. A., 2018, A Python Script for Aligning the STIS Echelle Blaze Function, Instrument Science Report STIS 2018-1, 13 pages
- Bagnulo S., Landstreet J. D., 2020, *A&A*, **643**, A134
- Bagnulo S., Landstreet J. D., 2021, *MNRAS*, **507**, 5902
- Bagnulo S., Landstreet J. D., 2022, *ApJ*, **935**, L12
- Bailer-Jones C. A. L., 2015, *PASP*, **127**, 994
- Becker A., Lorenzen W., Fortney J. J., Nettelmann N., Schöttler M., Redmer R., 2014, *ApJS*, **215**, 21
- Bédard A., 2024, *Ap&SS*, **369**, 43
- Bédard A., Bergeron P., Fontaine G., 2017, *ApJ*, **848**, 11
- Bédard A., Bergeron P., Brassard P., Fontaine G., 2020, *ApJ*, **901**, 93
- Bédard A., Brassard P., Bergeron P., Blouin S., 2022a, *ApJ*, **927**, 128
- Bédard A., Bergeron P., Brassard P., 2022b, *ApJ*, **930**, 8
- Berdyugin A. V., Piirola V., Bagnulo S., Landstreet J. D., Berdyugina S. V., 2022, *A&A*, **657**, A105
- Bergeron P., Ruiz M. T., Leggett S. K., 1997, *ApJS*, **108**, 339
- Bergeron P., Leggett S. K., Ruiz M. T., 2001, *ApJS*, **133**, 413

**Table 12.** Periods or variability limits from *TESS* data of 13 pc white dwarfs. *TESS-LOCALIZE* was applied to check if any signal originated from the white dwarf. An NOV of 1 means the source is not variable to 1 ppt (part-per-thousand), equivalent to 0.1 per cent amplitude. Magnetic field strengths are also listed (Bagnulo & Landstreet 2021)

WD name	$P_{\text{rot}}$ (hr)	NOV (ppt)	Magnetic field strength (MG)
0009+501	8.02	[2.5 ppt amp. spot]	0.25
0038–226	–	1	–
0046+051	–	0.2	–
0135–052	–	0.2	–
0141–675	–	0.2	–
0208–510	–	Field too crowded	–
0245+541	–	1	–
0310–688	–	0.1	–
0413–077	–	Field too crowded	–
0426+588	–	Field too crowded	–
0435–088	–	0.5	–
0548–001	–	0.5	7
0552–041	–	0.5	–
0553+053	–	1.5	15
0642–166	–	Field too crowded	–
0727+482 A	–	0.3	–
0727+482 B	–	0.3	–
0736+053	–	Field too crowded	–
0738–172	–	0.3	–
0752–676	–	0.1	–
0810–353	–	1	30
0821–669	–	0.4	–
0839–327	–	Signal not from WD	–
0912+536	31.95	[19.2 ppt amp. spot]	100
1055–072	–	No <i>TESS</i> data available	–
1132–325	–	Field too crowded	–
1142–645	–	Signal not from WD	–
1202–232	–	0.2	–
1334+039	–	0.7	–
1345+238	–	1.5	–
1620–391	–	Signal not from WD	–
1630+089	–	No <i>TESS</i> data available	–
1647+591	9.1	[1.8 ppt amp. pulsations]	–
1748+708	–	0.1	300
1900+705	–	0.1	200
1917–077	–	1	–
1917+386	–	0.6	–
1953–011	34.62	[25.0 ppt amp. spot]	0.5
2140+207	–	0.4	–
2150+591	–	Field too crowded	0.8
2251–070	–	1.5	–
2359–434	2.695	[3.7 ppt amp. spot]	0.1

Bergeron P., Dufour P., Fontaine G., Coutu S., Blouin S., Genest-Beaulieu C., Bédard A., Rolland B., 2019, *ApJ*, **876**, 67

Bergeron P., Kilic M., Blouin S., Bédard A., Leggett S. K., Brown W. R., 2022, *ApJ*, **934**, 36

Blouin S., 2022, *A&A*, **666**, L7

Blouin S., Dufour P., 2019, *MNRAS*, **490**, 4166

Blouin S., Kowalski P. M., Dufour P., 2017, *ApJ*, **848**, 36

Blouin S., Dufour P., Allard N. F., 2018, *ApJ*, **863**, 184

Blouin S., Dufour P., Allard N. F., Salim S., Rich R. M., Koopmans L. V. E., 2019a, *ApJ*, **872**, 188

Blouin S., Allard N. F., Leininger T., Gadéa F. X., Dufour P., 2019b, *ApJ*, **875**, 137

Blouin S., Dufour P., Thibeault C., Allard N. F., 2019c, *ApJ*, **878**, 63

Blouin S., Kilic M., Bédard A., Tremblay P.-E., 2023, *MNRAS*, **525**, L112

Blouin S., Kilic M., Albert L., Azartash-Namin B., Dufour P., 2024, *ApJ*, **976**, 218

Bognár Z., Sódor Á., 2024, *A&A*, **684**, A76

Bohlin R. C., Deustua S. E., de Rosa G., 2019, *AJ*, **158**, 211

Bond H. E., et al., 2015, *ApJ*, **813**, 106

Bond H. E., et al., 2017a, *ApJ*, **840**, 70

Bond H. E., Bergeron P., Bédard A., 2017b, *ApJ*, **848**, 16

Borysov A., Jorgensen U. G., Fu Y., 2001, *J. Quant. Spectrosc. Radiative Transfer*, **68**, 235

Buchan A. M., Bonsor A., Shorttle O., Wade J., Harrison J., Noack L., Koester D., 2022, *MNRAS*, **510**, 3512

Buchan A. M., Tremblay P.-E., Bédard A., Bauer E. B., Cunningham T., 2025, *MNRAS*, **544**, 2098

Camisassa M., Torres S., Hollands M., Koester D., Raddi R., Althaus L. G., Rebassa-Mansergas A., 2023, *A&A*, **674**, A213

Caron A., Bergeron P., Blouin S., Leggett S. K., 2023, *MNRAS*, **519**, 4529

Coutu S., Dufour P., Bergeron P., Blouin S., Loranger E., Allard N. F., Dunlap B. H., 2019, *ApJ*, **885**, 74

Cukanovaite E., Tremblay P.-E., Bergeron P., Freytag B., Ludwig H.-G., Steffen M., 2021, *MNRAS*, **501**, 5274

Cunningham T., Tremblay P.-E., Freytag B., Ludwig H.-G., Koester D., 2019, *MNRAS*, **488**, 2503

Cunningham T., et al., 2021, *MNRAS*, **503**, 1646

Cunningham T., Tremblay P.-E., W. O'Brien M., 2024, *MNRAS*, **527**, 3602

Debes J. H., et al., 2025, *AJ*, **170**, 123

Dufour P., 2011, in Hoard D. W., ed., , White Dwarf Atmospheres and Circumstellar Environments. WILEY-VCH Verlag GmbH and Co, pp 53–88, doi:10.48550/arXiv.1109.6849

Dufour P., Bergeron P., Fontaine G., 2005, *ApJ*, **627**, 404

Dufour P., Liebert J., Fontaine G., Behara N., 2007, *Nature*, **450**, 522

Dufour P., Blouin S., Coutu S., Fortin-Archambault M., Thibeault C., Bergeron P., Fontaine G., 2017, in Tremblay P. E., Gänsicke B., Marsh T., eds, Astronomical Society of the Pacific Conference Series Vol. 509, 20th European White Dwarf Workshop. p. 3 (arXiv:1610.00986)

Elms A. K., Tremblay P.-E., Gänsicke B. T., Koester D., Hollands M. A., Gentile Fusillo N. P., Cunningham T., Apps K., 2022, *MNRAS*, **517**, 4557

Elms A. K., et al., 2024, *MNRAS*, **534**, 2758

Farihi J., Bond H. E., Dufour P., Haghighipour N., Schaefer G. H., Holberg J. B., Barstow M. A., Burleigh M. R., 2013, *MNRAS*, **430**, 652

Ferrario L., de Martino D., Gänsicke B. T., 2015, *Space Sci. Rev.*, **191**, 111

Freudling W., Romaniello M., Bramich D. M., Ballester P., Forchi V., García-Dabó C. E., Moehler S., Neeser M. J., 2013, *A&A*, **559**, A96

Gaia Collaboration et al., 2021, *A&A*, **649**, A1

Gänsicke B. T., Koester D., Farihi J., Girven J., Parsons S. G., Breedt E., 2012, *MNRAS*, **424**, 333

Gänsicke B. T., et al., 2015, An HST legacy ultraviolet spectroscopic survey of the 13pc white dwarf sample, HST Proposal. Cycle 23, ID. #14076

Gänsicke B. T., Koester D., Farihi J., Tozola O., 2018, *MNRAS*, **481**, 4323

Genest-Beaulieu C., Bergeron P., 2019, *ApJ*, **871**, 169

Gentile Fusillo N. P., Tremblay P. E., Jordan S., Gänsicke B. T., Kalirai J. S., Cummings J., 2018, *MNRAS*, **473**, 3693

Gentile Fusillo N. P., et al., 2021, *MNRAS*, **508**, 3877

Giammichele N., Bergeron P., Dufour P., 2012, *ApJS*, **199**, 29

Hall P. B., Maxwell A. J., 2008, *ApJ*, **678**, 1292

Hardy F., Dufour P., Jordan S., 2023a, *MNRAS*, **520**, 6111

Hardy F., Dufour P., Jordan S., 2023b, *MNRAS*, **520**, 6135

Hare W. F. J., Welsh H. L., 1958, *Canadian Journal of Physics*, **36**, 88

Harrison J. H. D., Bonsor A., Madhusudhan N., 2018, *MNRAS*, **479**, 3814

Harrison J. H. D., Bonsor A., Kama M., Buchan A. M., Blouin S., Koester D., 2021, *MNRAS*, **504**, 2853

Higgins M. E., Bell K. J., 2023, *AJ*, **165**, 141

Holberg J. B., Oswalt T. D., Sion E. M., 2002, *ApJ*, **571**, 512

Holberg J. B., Sion E. M., Oswalt T., McCook G. P., Foran S., Subasavage J. P., 2008, *AJ*, **135**, 1225

Hollands M. A., Koester D., Alekseev V., Herbert E. L., Gänsicke B. T., 2017, *MNRAS*, **467**, 4970

Hollands M. A., Gänsicke B. T., Koester D., 2018a, *MNRAS*, **477**, 93

- Hollands M. A., Tremblay P. E., Gänsicke B. T., Gentile-Fusillo N. P., Toonen S., 2018b, *MNRAS*, **480**, 3942
- Hollands M. A., Tremblay P. E., Gänsicke B. T., Koester D., 2022, *MNRAS*, **511**, 71
- Huang B., et al., 2024, *ApJS*, **271**, 13
- Hummer D. G., Mihalas D., 1988, *ApJ*, **331**, 794
- Iglesias C. A., Rogers F. J., Saumon D., 2002, *ApJ*, **569**, L111
- Jura M., Xu S., Klein B., Koester D., Zuckerman B., 2012, *ApJ*, **750**, 69
- Kaiser B. C., Clemens J. C., Blouin S., Dennihy E., Dufour P., Hegedus R. J., Reding J. S., 2025, *ApJ*, **979**, 111
- Kausch W., et al., 2015, *A&A*, **576**, A78
- Kemp J. C., Swedlund J. B., Landstreet J. D., Angel J. R. P., 1970, *ApJ*, **161**, L77
- Kilic M., Bergeron P., Blouin S., Moss A., Brown W. R., Bédard A., Jewett G., Agüeros M. A., 2025, *ApJ*, **979**, 157
- Kilic M., et al., 2026, arXiv e-prints, p. arXiv:2606.25377
- Koester D., 2010, *Mem. Soc. Astron. Italiana*, **81**, 921
- Koester D., Kepler S. O., 2019, *A&A*, **628**, A102
- Koester D., Wolff B., 2000, *A&A*, **357**, 587
- Koester D., et al., 2001, *A&A*, **378**, 556
- Koester D., Gänsicke B. T., Farihi J., 2014, *A&A*, **566**, A34
- Koester D., Kepler S. O., Irwin A. W., 2020, *A&A*, **635**, A103
- Kowalski P. M., 2010, *A&A*, **519**, L8
- Kowalski P. M., 2014, *A&A*, **566**, L8
- Kowalski P. M., 2026, *A&A*, **708**, A26
- Kowalski P. M., Saumon D., 2006, *ApJ*, **651**, L137
- Kowalski P. M., Mazevet S., Saumon D., Challacombe M., 2007, *Phys. Rev. B*, **76**, 075112
- Kramida A., Ralchenko Y., Nave G., Reader J., 2018, in *APS Division of Atomic, Molecular and Optical Physics Meeting Abstracts*. p. M01.004
- Lajoie C.-P., Bergeron P., 2007, *ApJ*, **667**, 1126
- Limbach M. A., et al., 2024, *ApJ*, **973**, L11
- Limoges M. M., Lépine S., Bergeron P., 2013, *AJ*, **145**, 136
- McCleery J., et al., 2020, *MNRAS*, **499**, 1890
- McGill P., et al., 2023, *MNRAS*, **520**, 259
- Mihalas D., Hummer D. G., Mihalas B. W., Daepfen W., 1990, *ApJ*, **350**, 300
- Munday J., et al., 2024, *MNRAS*, **532**, 2534
- Napiwotzki R., et al., 2020, *A&A*, **638**, A131
- Neale L., Tennyson J., 1995, *ApJ*, **454**, L169
- O'Brien M. W., et al., 2023, *MNRAS*, **518**, 3055
- O'Brien M. W., et al., 2024, *MNRAS*, **527**, 8687
- O'Brien M. W., Tremblay P.-E., Klein B. L., Melis C., Koester D., Buchan A. M., Veras D., Doyle A. E., 2025, *MNRAS*, **539**, 171
- Oliveira da Rosa G., Kepler S. O., Soethe L. T. T., Romero A. D., Bell K. J., 2024, *ApJ*, **974**, 314
- Oswalt T. D., Sion E. M., Hammond G., Vauclair G., Liebert J. W., Wegner G., Koester D., Marcum P. M., 1991, *AJ*, **101**, 583
- Ould Rouis L. B., et al., 2024, *ApJ*, **976**, 156
- Ould Rouis L. B., et al., 2026, *ApJ*, **999**, 146
- Provencal J. L., Shipman H. L., Wesemael F., Bergeron P., Bond H. E., Liebert J., Sion E. M., 1997, *ApJ*, **480**, 777
- Provencal J. L., Shipman H. L., Koester D., Wesemael F., Bergeron P., 2002, *ApJ*, **568**, 324
- Ramírez S. H., Gänsicke B. T., Koester D., Lafarga M., Gentile-Fusillo N. P., 2025, *MNRAS*, **539**, 2884
- Ricker G. R., et al., 2015, *Journal of Astronomical Telescopes, Instruments, and Systems*, **1**, 014003
- Rodrigo C., Solano E., 2020, in *XIV.0 Scientific Meeting (virtual) of the Spanish Astronomical Society*. p. 182
- Rodrigo C., Solano E., Bayo A., 2012, *SVO Filter Profile Service Version 1.0*, IVOA Working Draft 15 October 2012, doi:10.5479/ADS/bib/2012ivoa.rept.1015R
- Rogers L. K., et al., 2024, *MNRAS*, **527**, 977
- Rohrmann R. D., 2018, *MNRAS*, **473**, 457
- Saffer R. A., Liebert J., Olszewski E. W., 1988, *ApJ*, **334**, 947
- Sahu K. C., et al., 2017, *Science*, **356**, 1046
- Sahu S., et al., 2023, *MNRAS*, **526**, 5800
- Sahu S., Tremblay P.-E., Lallement R., Redfield S., Gänsicke B. T., 2024, *MNRAS*, **535**, 1147
- Sahu S., et al., 2025a, *Nature Astronomy*, **9**, 1347
- Sahu S., Tremblay P.-E., Koester D., O'Brien M. W., Blouin S., Gänsicke B. T., Fairchild V., 2025b, *MNRAS*, **544**, 2038
- Saumon D., Jacobson S. B., 1999, *ApJ*, **511**, L107
- Saumon D., Holberg J. B., Kowalski P. M., 2014, *ApJ*, **790**, 50
- Saumon D., Blouin S., Tremblay P.-E., 2022, *Phys. Rep.*, **988**, 1
- Seaton M. J., 1995, *The opacity project*. Bristol, UK ; Philadelphia : Institute of Physics Pub.
- Sion E. M., Greenstein J. L., Landstreet J. D., Liebert J., Shipman H. L., Wegner G. A., 1983, *ApJ*, **269**, 253
- Skrutskie M. F., et al., 2006, *AJ*, **131**, 1163
- Smette A., et al., 2015, *A&A*, **576**, A77
- Steen M., Hermes J. J., Guidry J. A., Paiva A., Farihi J., Heintz T. M., Ewing B. B., Berry N., 2024, *ApJ*, **967**, 166
- Subasavage J. P., Henry T. J., Bergeron P., Dufour P., Hambly N. C., Beaulieu T. D., 2007, *AJ*, **134**, 252
- Temminck K. D., Toonen S., Zapartas E., Justham S., Gänsicke B. T., 2020, *A&A*, **636**, A31
- Tennyson J., et al., 2016, *Journal of Molecular Spectroscopy*, **327**, 73
- Tennyson J., et al., 2024, *J. Quant. Spectrosc. Radiative Transfer*, **326**, 109083
- Toonen S., Hollands M., Gänsicke B. T., Boekholt T., 2017, *A&A*, **602**, A16
- Tremblay P. E., Bergeron P., 2009, *ApJ*, **696**, 1755
- Tremblay P. E., Bergeron P., Kalirai J. S., Gianninas A., 2010, *ApJ*, **712**, 1345
- Tremblay P. E., Bergeron P., Gianninas A., 2011, *ApJ*, **730**, 128
- Tremblay P.-E., Ludwig H.-G., Steffen M., Freytag B., 2013, *A&A*, **559**, A104
- Tremblay P. E., Gianninas A., Kilic M., Ludwig H. G., Steffen M., Freytag B., Hermes J. J., 2015a, *ApJ*, **809**, 148
- Tremblay P. E., Fontaine G., Freytag B., Steiner O., Ludwig H. G., Steffen M., Wedemeyer S., Brassard P., 2015b, *ApJ*, **812**, 19
- Tremblay P. E., Cummings J., Kalirai J. S., Gänsicke B. T., Gentile-Fusillo N., Raddi R., 2016, *MNRAS*, **461**, 2100
- Tremblay P. E., Cukanovaite E., Gentile Fusillo N. P., Cunningham T., Hollands M. A., 2019, *MNRAS*, **482**, 5222
- Tremblay P. E., et al., 2020, *MNRAS*, **497**, 130
- Vernet J., et al., 2011, *A&A*, **536**, A105
- Vincent O., Barstow M. A., Jordan S., Mander C., Bergeron P., Dufour P., 2024, *A&A*, **682**, A5
- Virtanen P., et al., 2020, *Nature Methods*, **17**, 261
- Walkup R. E., 1982, *Phys. Rev. A*, **25**, 596
- Weidemann V., Koester D., 1995, *A&A*, **297**, 216
- Weidemann V., Koester D., Vauclair G., 1980, *A&A*, **83**, L13
- Williams J. T., et al., 2025, *MNRAS*, **541**, 1377
- Wolff B., Koester D., Liebert J., 2002, *A&A*, **385**, 995
- Worthey G., Pal T., Khan I., Shi X., Bohlin R. C., 2022, *Scattered Light in STIS Grating G230LB*, Instrument Science Report STIS 2022-05, 26 pages
- Wright E. L., et al., 2010, *AJ*, **140**, 1868
- Zeidler-K. T. E. M., Koester D., 1982, *A&A*, **113**, 173
- Zuckerman B., Koester D., Reid I. N., Hünsch M., 2003, *ApJ*, **596**, 477
- van Leeuwen F., 2007, *A&A*, **474**, 653

This paper has been typeset from a  $\text{\LaTeX}$  file prepared by the author.